

Article

Cranial Material of Long-Snouted Dolphins (Cetacea, Odontoceti, Eurhinodelphinidae) from the Early Miocene of Rosignano Monferrato, Piedmont (NW Italy): Anatomy, Paleoneurology, Phylogenetic Relationships and Paleobiogeography

Vera Tosetto ¹, Piero Damarco ², Riccardo Daniello ², Marco Pavia ¹, Giorgio Carnevale ¹
and Michelangelo Bisconti ^{1,3,*} 

¹ Dipartimento di Scienze della Terra, Università degli Studi di Torino, via Valperga Caluso 35, 10125 Torino, Italy

² Ente di Gestione del Parco Paleontologico Astigiano, Museo Paleontologico Territoriale dell'Astigiano, Corso Vittorio Alfieri 381, 14100 Asti, Italy

³ San Diego Natural History Museum, 1788 El Prado, San Diego, CA 92101, USA

* Correspondence: michelangelo.bisconti@unito.it

Abstract: We provide a new study of previously published eurhinodelphinid materials from the early Miocene of Piedmont (NW Italy) based on a new preparation of the fossil specimens. We studied specimens previously assigned to *Tursiops miocaenus* and *Dalpiazella* sp. and provide new anatomical data on the eurhinodelphinid skull and ear bones. In particular, we suggest that a skull that was previously assigned to *Tursiops miocaenus* must be reassigned to *Ziphiodelphis sigmoideus* (Cetacea, Odontoceti, Eurhinodelphinidae) based on new comparisons of the squamosal. This finding enabled us to provide new anatomical information on the ear bone anatomy of *Z. sigmoideus* that was previously unknown. The material originally assigned to *Tursiops miocaenus* is currently lost. For this reason and due to the fact that the partial illustration of this species by Portis does not allow us to find diagnostic characters for this species, we decided that *Tursiops miocaenus* is a *nomen dubium*. Analysis of additional isolated teeth previously assigned to *Tursiops miocaenus* led to the conclusion that these specimens represent Odontoceti *incertae sedis*. We performed a new phylogenetic analysis by adding newly discovered character states to a previous dataset and a paleobiogeographic analysis of Eurhinodelphinidae. We found two monophyletic clades within this family. The paleobiogeographic pattern found by the present work suggests the existence of North Atlantic and Mediterranean clades with some species distributed among both basins. We analyzed the virtual endocast of *Ziphiodelphis sigmoideus* and found that it resembles that of *Schizodelphis* in several respects, suggesting that some of the more derived characters of the odontocete brain were still absent in these early Miocene eurhinodelphinids.

Keywords: brain evolution; endocast; eurhinodelphinidae; miocene; paleobiogeography; piedmont; osteology; phylogeny



Citation: Tosetto, V.; Damarco, P.; Daniello, R.; Pavia, M.; Carnevale, G.; Bisconti, M. Cranial Material of Long-Snouted Dolphins (Cetacea, Odontoceti, Eurhinodelphinidae) from the Early Miocene of Rosignano Monferrato, Piedmont (NW Italy): Anatomy, Paleoneurology, Phylogenetic Relationships and Paleobiogeography. *Diversity* **2023**, *15*, 227. <https://doi.org/10.3390/d15020227>

Academic Editor: Bert W. Hoeksema

Received: 9 December 2022

Revised: 25 January 2023

Accepted: 31 January 2023

Published: 5 February 2023



Copyright: © 2023 by the authors. Licensee MDPI, Basel, Switzerland. This article is an open access article distributed under the terms and conditions of the Creative Commons Attribution (CC BY) license (<https://creativecommons.org/licenses/by/4.0/>).

1. Introduction

Numerous fossil cetaceans have been discovered in Italy in the last three centuries, especially in Piedmont, Tuscany, and Emilia Romagna, and in some more restricted areas, such as those close to the cities of Belluno, Lecce, and Ragusa [1]. In Piedmont, the local geological history was characterized by a series of Miocene and Pliocene paleoenvironments with remarkable biodiversity, especially of cetaceans [2]. The fossil record of cetaceans in Piedmont, which is in large part preserved in the collection of the Museo Paleontologico Territoriale dell'Astigiano (hereinafter MPTA) [3], contributes to the reconstruction of

the main evolutionary trends of these marine mammals in the Mediterranean Miocene, providing crucial information for the reconstruction of the taxonomic changes and turnover patterns that affected the cetacean communities of the central Mediterranean area during the Neogene [4]. In this basin, the odontocete diversity has consistently increased from the latest Aquitanian-early Burdigalian to reach a peak in diversity during the Burdigalian-Langhian [4]. This early Miocene Mediterranean odontocete fauna was characterized by the prevalence of longirostrine species, which lived in estuarine and coastal environments [4].

The Monferrato area (which includes the SE portion of the Piedmont region (Asti and Alessandria provinces) is characterized by two stratigraphic sequences related to different tectonostratigraphic domains, emerging in western and eastern portions, respectively. In particular, the succession of the eastern Monferrato (Oligocene-lower Miocene) consists of terrigenous sediments of variable thickness, which are covered by shallow-water shelf carbonates [5]. These include several units, among which the Pietra da Cantoni Formation (hereinafter PdC) occupies the uppermost portion. A number of fossil cetaceans were found in the PdC (which is Burdigalian-upper Langhian in age) over the last three centuries [3]. The PdC accumulated in an outer subsiding carbonate platform and slope, being characterized by a transgressive trend and a deepening of the basin from east to west. The fossil cetofauna of this formation is primarily represented by tympanic bullae, periotics, teeth, and internal skull models referred to as four odontocete superfamilies, namely, the Physterioidea (at least five physterid genera have been recognized based on isolated periotics [4,6]), Squalodontoidea, Delphinoidea, and Platanistoidea; in addition, specimens referred to the family Ziphiidae were identified [4,6].

Apart from these fragmentary remains, a partial skull (Museo di Geologia e Paleontologia dell'Università degli Studi di Torino, hereinafter MGPT-PU; specimen MGPT-PU 13881/1-2) of an early Miocene odontocete was found in a PdC outcrop at Rosignano Monferrato (approximately 80 Km ESE from Torino; Figure 1) and formerly reported by Parona [7]. This skull is one of the more complete specimens coming from the early Miocene of Piedmont and also includes the ear bones (both periotics and bullae) and parts of the mandible. The specimen pertains to the collection of MGPT and is currently housed at MPTA in Asti. The history of this find is outlined below.

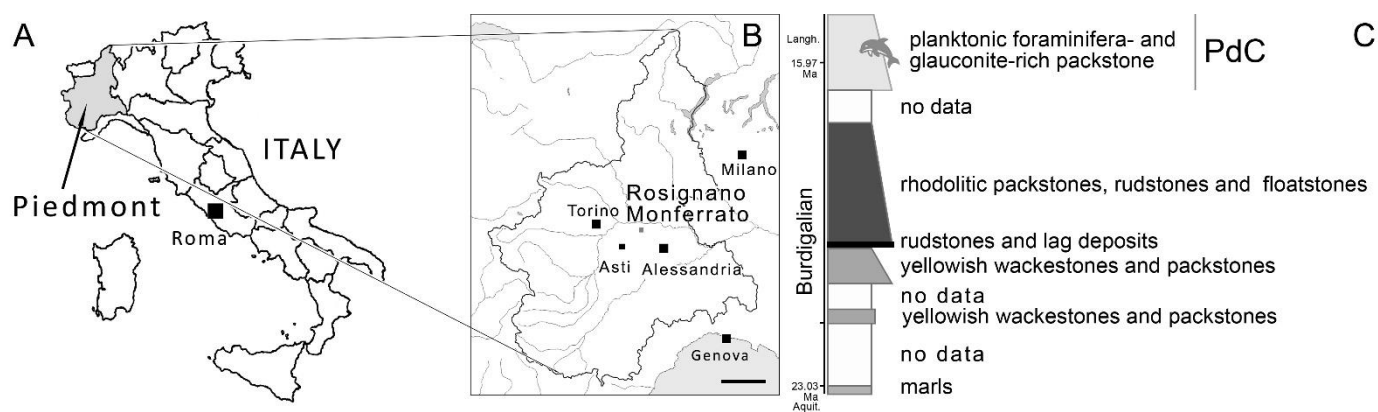


Figure 1. Locality of the discovery of MGPT-PU 13881/-4. (A) Italian peninsula with Piedmont highlighted in gray. (B) Piedmont showing Rosignano Monferrato. Scale bar equals 50 km. (C) Scheme of the stratigraphic column at Rosignano Monferrato showing the principal lithologies, the occurrence of MGPT-PU 13881/-4, and a chronological scale in million years (Ma). Caption: Aquit., Aquitanian; Langh., Langhian; PdC, Pietra da Cantoni. The dolphin icon indicates the approximate position of the find in the stratigraphic column.

Portis [8] established *Tursiops miocaenus* based on six young teeth mistreated and broken found in the PdC near Rosignano (Figure 2). In Portis' view, the inclusion of this specimen in *Tursiops* represented evidence supporting the idea that the evolutionary history

of the bottlenose dolphin had its roots in the Miocene. Portis [8] was cited incorrectly in subsequent studies that referred to him when the fossils were reported by Parona [7]. Parona [7] reported the discovery of new odontocete remains from the PdC in Rosignano, which he referred to as *Tursiops miocenus*. The fossils were part of the important collection assembled by Filippo Cantamessa and acquired by the Museo di Geologia e Paleontologia of the University of Torino. Parona prepared and examined the specimen, providing a list and a description of all of the available fragments that are redescribed in detail herein (partial skull, fragment of a mandible with three teeth, a single isolated tooth, and right and left ear bones) [7]. Parona pointed out that these teeth, although smaller, correspond in morphology to those previously described by Portis, therefore supporting its attribution to *Tursiops miocaenus* Portis, 1885 [7].



Figure 2. Excerpt from Portis (1885) [8] plate IX (Figure 106a,b) representing two of the teeth assigned to *Tursiops miocaenus* by Portis.

At the time, during the preparatory work, an accurate micropaleontological analysis of the sediment was carried out, primarily based on foraminiferans, which allowed researchers to define the age of fossils and correlate them with the paleontological content of other Italian Miocene formations [7]. Parona was no longer mentioned by subsequent studies (e.g., [1,6,9]), which attributed the discovery and the various fragments to Portis [6]; it should be noted that in the later studies, only some of the fragments listed above were considered [1,6]. In the present paper, for the first time after more than one century, the work of Parona [7] is rediscovered and it is used to reconstruct the taxonomic history of the skull MGPT-PU 13881/1.

Pilleri and co-workers assigned the specimen to *Dalpiazella* sp., a genus included within Delphinidae [6]. They described the skull fragment (MGPT-PU 13881/1) with the right tympanic bulla in situ, and a left tympanic bulla (MGPT-PU 13881/2) (Table 1). However, they did not describe the three-toothed fragment cited in ref. [7] and stated that the teeth were not preserved.

Table 1. Specimens studied in the present paper.

SPECIMEN	NUMBER	REVISED TAXONOMY
rostrum fragment including three teeth	MGPT-PU 13881/3	Odontoceti <i>Incertae sedis</i>
isolated tooth	MGPT-PU 13881/4	
partial skull	MGPT-PU 13881/1	Eurhinodelphinidae Abel, 1901 <i>Ziphiodelphis</i> Dal Piaz, 1908 <i>Ziphiodelphis sigmoideus</i> Pilleri, 1985
fragment of left mandible	MGPT-PU 13881/1	
left tympanic bulla	MGPT-PU 13881/2	
right tympanic bulla	MGPT-PU 13881/2	
right periotic	MGPT-PU 13881/2	
left periotic	MGPT-PU 13906	

In a subsequent revision, Bianucci and coworkers removed the specimen from the family Delphinidae and assigned it to *Eurhinodelphis* [1]. In that work, the incomplete skull (MGPT-PU 13881/1-2) was described and the right tympanoperiotic complex was removed from the skull using acid treatment. According to ref. [1], the detached right periotic is identical to a left periotic (MGPT-PU 13906) that had been previously assigned to the Squalodontidae ([6], their pl. 3). Therefore, in ref. [1], it was suggested that MGPT-PU 13881/1-2 and MGPT-PU 13906 belong to the same individual and that the tympanoperiotic morphology perfectly agrees with that of the Eurhinodelphinidae described in previous studies [10–12]. Such taxonomic attribution was corroborated by considering the size and shape of the skull, the morphology and relatively large size of the periotic, and the presence, on the tympanic bulla, of a deep and long ventral sulcus that slopes on its anterior side laterally [1]. Unfortunately, however, the specimen was not fully prepared at the time of that publication, and most of the dorsal and ventral surfaces were still obliterated by the matrix, which is a porous limestone characterized by a millimeter granular texture. The matrix is distinguishable from the bone by color, luster, and degree of surface smoothness.

In 2021 and 2022, the specimen underwent a new preparation process (by two of us: VT and PD) that allowed a better observation of the dorsal, ventral, and lateral views of the skull (Figures 3–6). This allowed us to carry out a detailed description and comparative analysis, which were virtually impossible in the past. In the present paper, therefore, the specimen is described and compared with a large record of early Miocene odontocetes, and its phylogenetic and paleobiogeographic relationships are investigated. Interestingly, the preparation of the specimen revealed that the dorsal surface of the neurocranium (including most of the supraoccipital and parietal) is missing so now the cerebral cavity can be visually explored. This allowed the preparation of a virtual endocast of the lateral and ventral surfaces of the brain together with a number of roots of cranial nerves. The comparative paleoneurology of the specimen is also included in this paper, and the neurological characters are discussed in the broader context of odontocete brain and cranial nerve evolution.

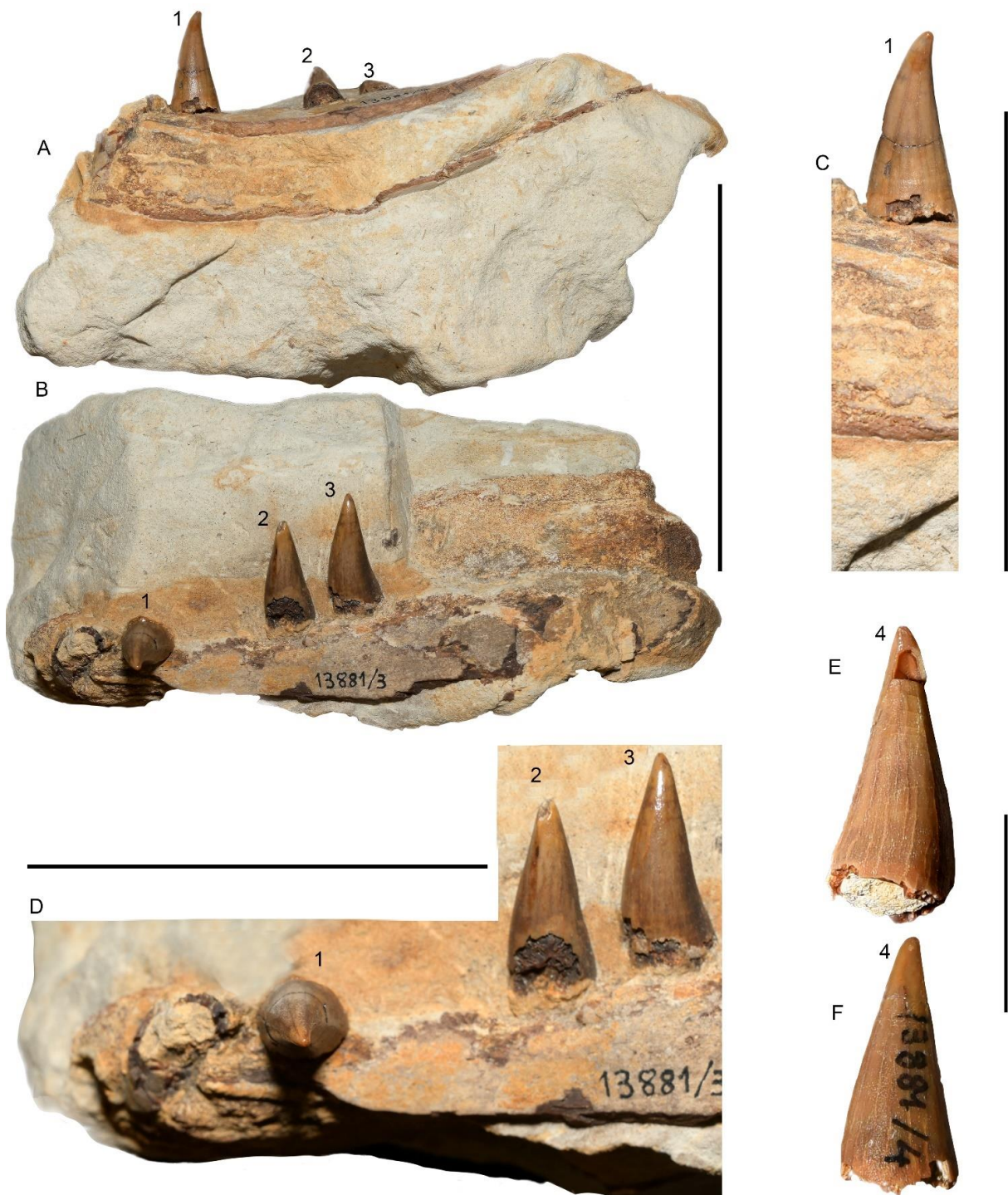


Figure 3. Dentition and mandibular fragments MGPT-PU 13881/3-4. (A) fragment with three teeth in ventral view (MGPT-PU 13881/3). (B) The same in lateral view. (C) Close-up view of the most anterior tooth (tooth 1) of those illustrated in (A). (D) Close-up view of the more posterior couple of teeth (teeth 2 and 3) of those illustrated in (A). Scale bars in (A–D) equal 5 cm. (E) Close-up view of MGPT-PU 13881/4 showing tooth 4 in lingual view. Scale bar in (E) equals 2 cm. (F) the same tooth in labial view.

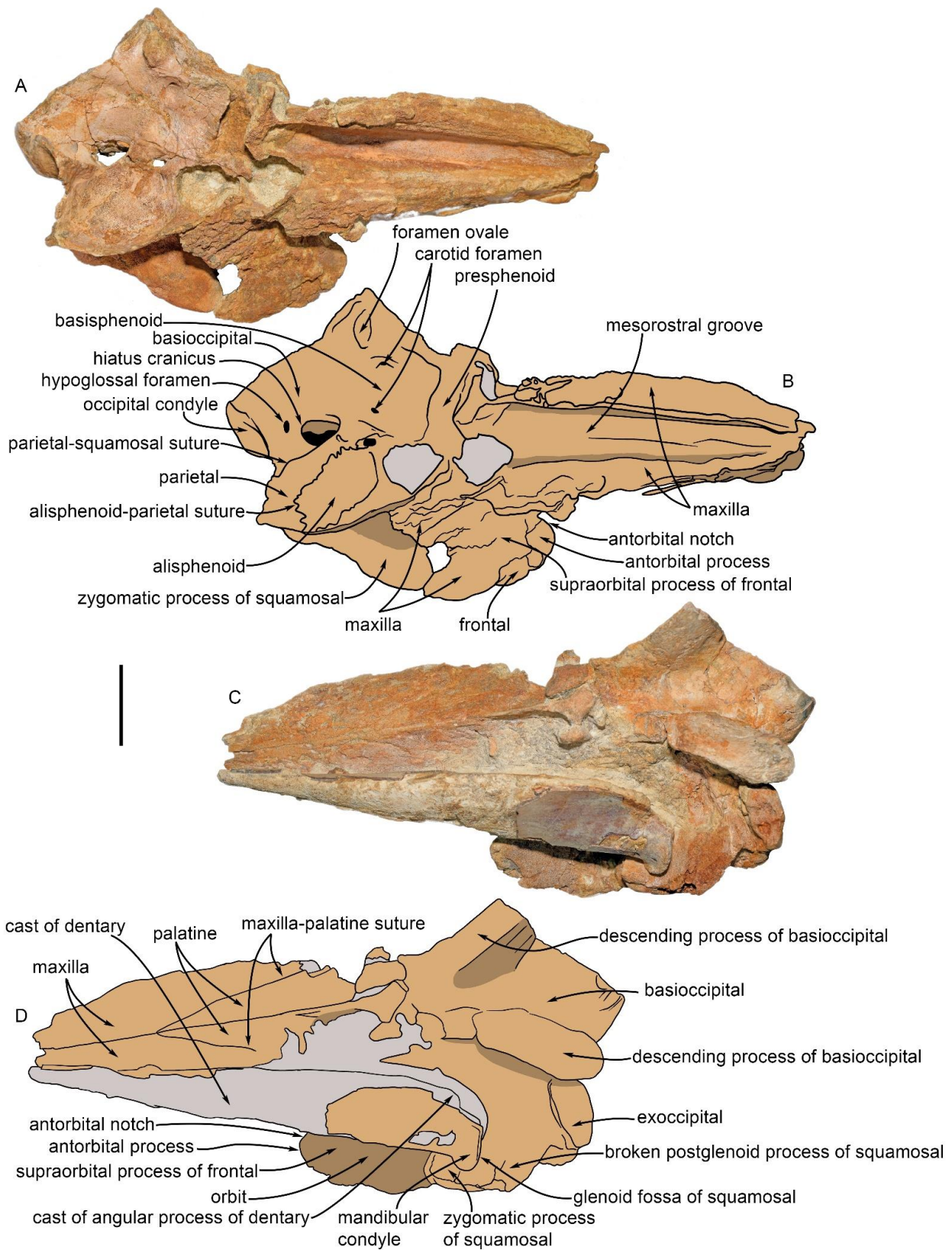


Figure 4. The partial skull MGPT-PU 13881/1 after preparation. (A) photographic representation of the skull in dorsal view. (B) Anatomical interpretation of (A). (C) Photographic representation of the skull in ventral view. (D) Anatomical interpretation of (C) Scale bar equals 5 cm.

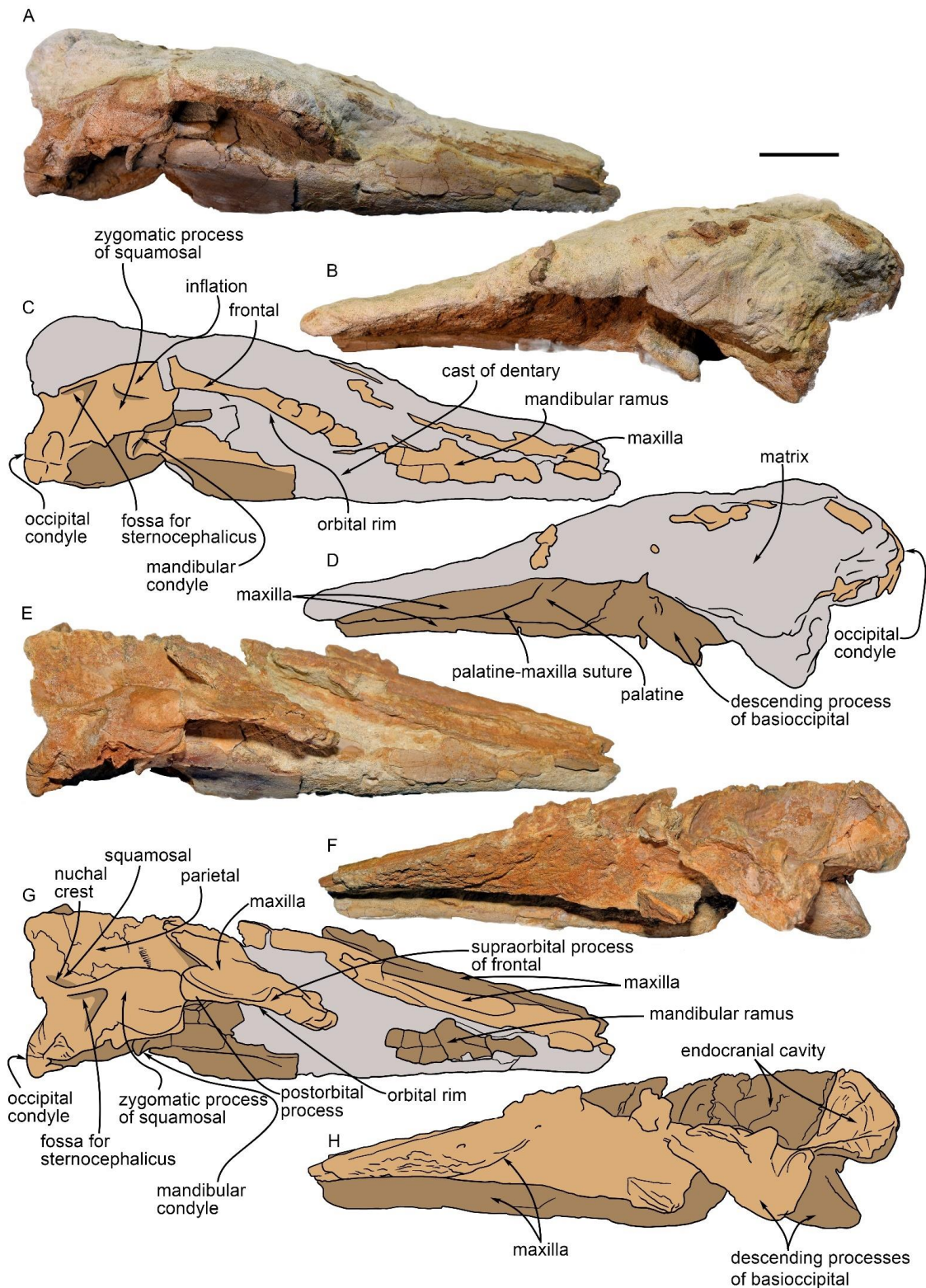


Figure 5. The partial skull MGPT-PU 13881/1 in lateral view. (A) Photographic representation of the skull before preparation in right lateral view. (B) Photographic representation of the skull before preparation in left lateral view. (C) Anatomical interpretation of (A). (D) Anatomical interpretation of (C). (E) Photographic representation of the skull after preparation in right lateral view. (F) Anatomical interpretation of (E). (G) Photographic representation of the skull after preparation in left lateral view. (H) Anatomical interpretation of (G). Scale bar equals 5 cm.

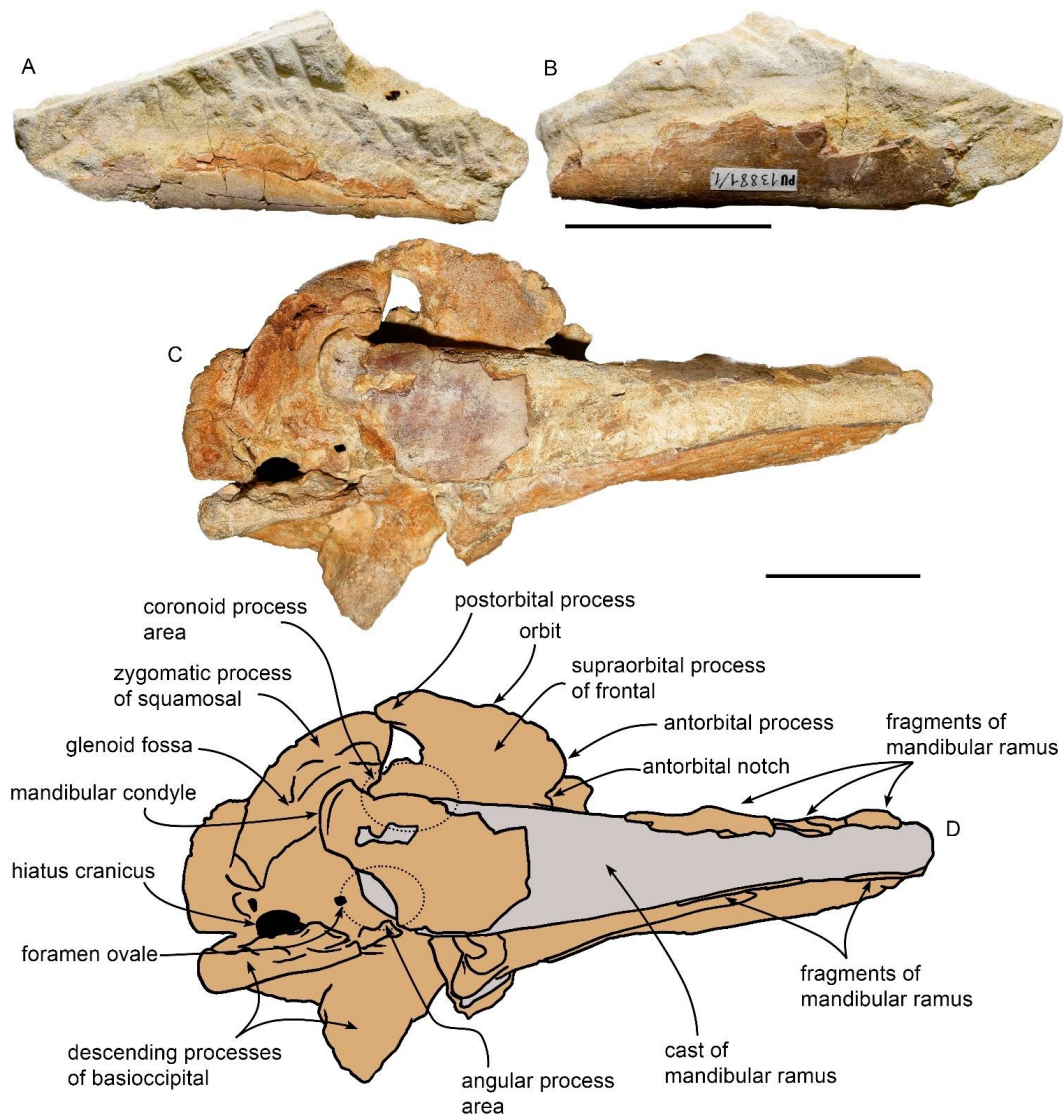


Figure 6. Mandibular morphology of MGPT-PU 13881/1. (A) Separated mandibular fragment belonging to the partial skull MGPT-PU 13881 in lateral view. (B) The same in medial view. (C) Photographic representation of the skull MGPT-PU 13881 in right ventrolateral view showing the right dentary orthogonally to its anteroposterior axis. (D) Anatomical interpretation of (C). Scale bar equals 5 cm.

2. Materials and Methods

2.1. Institutional Abbreviations

IRSNB: Institut Royal des Sciences Naturelles de Belgique, Bruxelles; MGPT-PU: Museo di Geologia e Paleontologia dell'Università degli Studi di Torino, Torino, Italia; MGP-PD: Museo di Geologia e Paleontologia dell'Università di Padova, Italia; MHNL: Muséum d'Histoire Naturelle de Lyon, France; MNHN: Museum National d'Histoire Naturelle, Paris, France; MPTA: Museo Paleontologico Territoriale dell'Astigiano, Asti, Italia; OU: University of Otago, Dunedin, New Zealand; PGN: Palaeontological collections of Montpellier University, France; USNM: United States National Museum of Natural History, Smithsonian Institution, Washington, DC, USA.

2.2. Studied Material

We studied the specimens listed in Table 1, which include a partial eurhinodelphinid skull and mandibular fragment (MGPT-PU 13881/1); left tympanoperiotic complex (includ-

ing left periotic and tympanic bulla) and right periotic (MGPT-PU 13881/2); left periotic (MGPT-PU 13906); a rostrum fragment including three isolated teeth (MGPT-PU 13881/3); and an isolated tooth (MGPT-PU 13881/4). Note that MGPT-PU 13881/1, 13881/2, and 13906 represent the same individual.

2.3. Preparation of the Skull MGPT-PU 13881/1

Until 2020, the dorsal surface of the skull MGPT-PU 13881/1 was covered by the original sedimentary matrix but with a largely exposed mandibular ramus (Figure S1 in Supplementary Material). The sedimentary matrix consists of a hard marl that is rich in glauconite and can be referenced to the early Miocene PdC complex. The bony tissue appeared to be very delicate, similar to other fossils found in the PdC Formation.

The preparation process was carried out in different steps bearing in mind the delicate nature of the specimen. The first step consisted of the application of mechanical preparation procedures allowing us to remove the majority of the matrix; during this process, cyanoacrylic glue was used to consolidate the bony tissue of the more delicate bones.

The second preparation step started after the matrix was reduced to a uniform 5 mm layer over the bones. A drill with a diamond cutter was used to remove the last covering matrix. Then, the remaining matrix was dissolved using an HCl solution at a dilution of 50%. Subsequently, the dilution was lowered to 10% and its application was stopped when the bones started to appear. The acid did not attack the bone because it was directed to remove the calcareous component of the matrix and not the phosphatic component of the bone itself. The removal of the sedimentary matrix resulted in the exposition of the basicranium.

The third preparation step included several washing iterations of the specimen and 12 h immersion of the skull in a solution of water and Ca bicarbonate (10% of dilution) to eliminate HCl residuals. The specimen was dried in open air. Finally, three iterations of the Paraloid B72 acrylic resin acetone-diluted solution were distributed to consolidate the skull. The first and second iterations included Paraloid with 5% dilution to allow a higher capacity of penetration into the bone; in the third iteration, Paraloid with 20% dilution was used to allow higher surface consolidation.

2.4. Anatomical Terminology, Photography, and Measurements

Anatomical terminology follows ref. [13]. The specimen was photographed by a full-frame DSLR Nikon D750 with a Tamron 11–30 mm VC USD lens and by a Nikon E5700. Measurements were taken using a Tacklife D02 digital caliper (150 mm) to the nearest 0.01 mm.

2.5. Body Size Estimate

It is possible to infer the transverse diameter of the foramen magnum as its ventral border is almost completely preserved and the transverse diameter of the occipital condyle is known (30 mm, see above). By using dedicated digital instruments in Adobe Photoshop and the transverse diameter of the occipital condyle as a scale, we inferred a value of 22.97 (c. 23) mm for the maximum transverse diameter of the foramen magnum. The maximum transverse diameter of the foramen magnum can be used to infer the occipital breadth of the specimen via the following regression-based equation [14]:

$$(1) \quad \text{Occipital breadth} = 3.057(\text{width of foramen magnum}) - 23.206$$

We then used the occipital breadth to infer the total body mass of the specimen by using the following formula [15]:

$$(2) \quad \text{Body mass} = 4.924(10^{-6})(\text{occipital breadth})^{3.858}$$

The body mass can be used to infer the total skeletal length by using the following formula developed by [16]:

$$(3) \quad \text{Log}(\text{body mass}) = 3.08(\text{log}(\text{skeletal length})) - 4.84.$$

2.6. Reconstruction of Virtual Endocast and Basicranium

The lack of the supraoccipital and most of the parietal from the dorsal surface of the skull allows direct observation of the endocranial cavity. We used digital photogrammetry to obtain a 3D rendering of the complex basicranial surface and the virtual endocast. Photogrammetry is still a rather underused technique in paleontology even though it is perfectly suited to acquiring and studying fossil specimens [17]; in this study, we used photogrammetry to reconstruct (1) a high-resolution 3D model of the skull, including the endocranial surface, and (2) a digital endocranial cast.

We acquired images from all possible angles of the basicranium after completing the specimen preparation, in order to perform SfM (Structure from Motion) photogrammetry, generate a digital version of the fossil, and, eventually, a virtual endocast of the endocranial space. Our photogrammetry/3D pipeline is based entirely on two open-source software (Meshroom and Blender), and it can be divided into three main phases explained below:

- A) Image acquisition was performed with a Smartphone quad-camera, which was more agile in the tight constraints of the endocranial space than a relatively bulkier digital camera. The main camera has a resolution of 64 MP and an f-value of 1.8 while the macro camera used for close up-details has a resolution of 5 MP and f/2.4. We gathered 705 pictures from different angles, 470 using the main camera and 235 with the macro.
- B) Model generation proceeded by loading the pictures without any need for post-processing in Meshroom in four iterations via Meshroom's "Augment Reconstruction" function. At the end of the fourth iteration, we generated a six-million-polygon model; this raw output was still affected to a certain extent by noise and visual artifacts (small holes, detached geometries, or intersecting faces), which required further processing.
- C) The mesh refinement was performed in Blender. Although Meshroom node-based functions could be used for mesh refinement, for example, with a commonly used "Decimate Node", we opted for Blender as it shares many mesh-related functionalities while also providing far greater control. In Blender's Edit Mode, we deleted detached parts of the mesh generated from the noise, dissolved degenerate geometries, and patched small missing surfaces. We also reduced the total polygon count with the "Decimate" modifier, reaching a total of 638,994 faces, providing better loading times without compromising the detail. With the refined mesh, we generated UV maps; it was now possible to import the file back into Meshroom and finalize the model with Texture generation.
- D) In Blender, we used the digital replica of MGPT-PU13881/1 basicranium as the equivalent of a mold by employing a "Boolean Modifier," which enables Boolean operations (such as the difference) between meshes. The second mesh we utilized as the cast material was a simple cube, which became our first version of the endocast. However, this version of the endocast was partially obscured by non-endocranial geometry originating from the space around the basicranium due to how Boolean operations work, which required manual removal through the Blender Edit Mode. Thanks to the final version of the endocast presented here, it has been possible to examine and reconstruct the nerves and various other adnexa at the base of the MGPT-PU13881 brain.

The photogrammetry-based 3D renderings of both the MGPT-PU 13881 skull and virtual endocast are freely available at Morphosource (project: https://www.morphosource.org/concern/biological_specimens/000493295, accessed on 23 February 2023; skull: <http://n2t.net/ark:/87602/m4/493298>, accessed on 23 February 2023; virtual basicranium and endocast: <http://n2t.net/ark:/87602/m4/493301>, accessed on 2 February 2023).

2.7. Phylogenetic Analysis

The phylogenetic analysis was realized based on a previously published dataset [18] to which we added 12 characters derived from our observations (characters 27–39). We coded the character states of MGPT-PU 13881/1-2 following published character descriptions [18,19]

and our own as presented in Table A1 of Appendix A. The new character states were coded following an outgroup comparison criterion (state 0 is that observed in at least one outgroup). The outgroup taxa included *Waipatia maerewhenua*, *Squalodon* spp., *Chilcacetus cavirhinus*, *Eoplatanista italica*, and *Iniopsis caucasica*. The resulting character x taxon matrix is shown in Table A2 of Appendix A and in Nexus format in Table S1 in the Supplementary Materials. We collapsed the two specimens used in ref. [18] to represent *Schizodelphis sulcatus* (i.e., PGN 2 and MNHNRL 12) into a single operational taxonomic unit named *Schizodelphis sulcatus*. We added *Chilcacetus cavirhinus*, *Vanbreenia trigonia*, and *Iniopsis caucasica* to the original matrix of ref. [18]; dismantled *Eurhinodelphis* in *E. bossi*, *E. cocheteuxi*, and *E. longirostris* and subdivided *Ziphiodelphis* in *Z. abeli* and *Z. sigmoideus* were added to the matrix as individual operational taxonomic units. Reference specimens are provided in Table A3 of Appendix A.

Inferences of phylogenetic trees were made using TNT 1.5 [20], an implicit enumeration exact search as implemented in the software. The consistency index (CI) and the Retention index (RI) were calculated by dedicated subroutines of TNT; the Homoplasy index (HI) was calculated using the following formula: $HI = 1 - CI$.

Node support was calculated in TNT by bootstrap (1000 replicates, traditional search with default parameters) and symmetric resampling (1000 replicates, absolute frequencies). We also provided the frequency of the clades observed in the strict consensus tree in the cladograms found by the exact search and mapped the synapomorphies at nodes via TNT-dedicated commands. The agreement between the phylogenetic pattern and the stratigraphic ages of the taxa was calculated using the stratigraphic consistency index (SCI; [21]).

2.8. Paleobiogeographic Analysis

We used the phylogenetic results to infer paleobiogeographic relationships via the reconstruction of ancestral geographic states at nodes. Geographic occurrences of the taxa are listed in Table 2. We used a maximum likelihood approach as implemented in Mesquite 3.61 [22] with the default Mk1 model to infer geographic occurrences at the internal nodes of Eurhinodelphinidae and used the probability values to formulate hypotheses of dispersal or vicariance events, explaining the geographic distribution of the studied species. This approach follows previously published guidelines [23,24].

Table 2. Geographic and stratigraphic occurrences of the eurhinodelphinid taxa used in the phylogenetic analysis. Data downloaded from Paleobiology Database (last accessed on 11 November 2022).

Species	Geographic Occurrence	Operational Geographic Unit	Stratigraphic Occurrence
<i>Eurhinodelphis bossi</i>	East United States Belgium Italy	NW Atlantic NE Atlantic Mediterranean	Burdigalian-Serravallian
<i>Eurhinodelphis cocheteuxi</i>	Belgium, Netherlands Belgium, Netherlands	NE Atlantic NE Atlantic	Aquitanian-Serravallian
<i>Eurhinodelphis longirostris</i>	Italy, Turkey East United States	Mediterranean NW Atlantic	Burdigalian-Tortonian
<i>Vanbreenia trigonia</i>	Netherlands	NE Atlantic	Langhian
<i>Mycteriacetus bellunensis</i>	Italy	Mediterranean	Aquitanian
<i>Xiphiacetus cristatus</i>	Belgium, Netherlands Italy	NE Atlantic Mediterranean	Burdigalian-Tortonian
<i>Schizodelphis morckhoviensis</i>	Austria	Paratethys	
<i>Schizodelphis barnesi</i>	Belgium	NE Atlantic	Langhian-Serravallian
	East United States	NW Atlantic	Burdigalian-Serravallian
<i>Schizodelphis sulcatus</i>	Austria, Switzerland Netherlands, Belgium East United States	Paratethys NE Atlantic NW Atlantic	Aquitanian-Tortonian
	Italy, France, Egypt	Mediterranean	
<i>Ziphiodelphis abeli</i>	Italy	Mediterranean	Aquitanian-Burdigalian
	Germany	NE Atlantic	
<i>Ziphiodelphis sigmoideus</i> (including MGPT 13881)	Italy	Mediterranean	Aquitanian-Burdigalian

3. Systematic Paleontology

Cetacea Brisson, 1762 [25]

Pelagiceti Uhen, 2008 [26]

Neoceti Fordyce and De Muizon, 2001 [27]

Odontoceti Flower, 1867 [28]

Incertae sedis

Material. A rostrum fragment including three teeth (teeth 1–3; MGPT-PU 13881/3) plus a single, isolated tooth (tooth 4; MGPT-PU 13881/4) (Table 1).

Locality and horizon. These specimens were ostensibly collected from the PdC exposure cropping out at Rosignano Monferrato. The sedimentary matrix clearly supports this hypothesis. The PdC Formation in the Rosignano Monferrato area has been referred to as the Burdigalian [5].

Description. A fragment of a tooth-bearing bone with three teeth partially immersed in a reddish sedimentary matrix (MGPT-PU 13881/3; Figure 3). The bony fragment is *c.* 15 cm in length and consists of a portion of a rostrum (likely a mandible) in which part of the reddish-brown bone is still preserved. The bone is recurved. In this section, the thin brown layer of the bone where the teeth insert continues curving even in the innermost part of the fragment gives rise to a cavity filled with darker limestone sediment. This is interpreted as a portion of the mandibular canal filled with sediment. The maximum height of this fragment is 24 mm on one side and 16 mm on the other, while its width (from the end of the preserved tooth row to the anterior end) is approximately 18 mm. On the outer edge of the left mandibular fragment, there are three complete teeth, two of which (first and second in Table 3) are adjacent and parallel (Figure 3A–D). The third tooth (third in Table 3) is isolated from the others and shows an orientation that is almost opposite to those of the other two. These teeth are of the same type and size, conical, sharp, and slightly curved, likely representing anterior elements (Table 3). These are characterized by a dark brown color and consist of a very thin, smooth, and shiny outer surface (corresponding to the enamel) with slight longitudinal streaks. The three teeth are damaged at their base, but do not show evidence of wear. A trace of the root can be seen but there is no evidence of their respective alveoli.

Table 3. Measurements of MGPT PU 13881/3-4 in mm.

Character	mm
MGPT PU 13881/3	
Maximum Length of partial mandible	140
Maximum width of partial mandible	16
Maximum height of partial mandible	24
Maximum height of tooth 1	18
Maximum transverse diameter of tooth 1 base	10
Maximum transverse diameter of tooth 1 apex	2
Maximum height of tooth 2	18
Maximum transverse diameter of tooth 2 base	10
Maximum transverse diameter of tooth 2 apex	2
Maximum height of tooth 3	18
Maximum transverse diameter of tooth 3 base	10
Maximum transverse diameter of tooth 3 apex	2
MGPT PU 13881/4	
Maximum height of tooth 4	18
Maximum width of tooth 4 base	10
Maximum width of tooth 4 apex	2

An additional, isolated tooth fragment (tooth 4; MGPT-PU 13881/4) shows the same morphological features of the three teeth associated with the rostrum fragment (Figure 3E,F). It is sharp, conical, and slightly curved; its length is 18 mm, while its basal diameter is 10 mm; the maximum diameter at the tip is 2 mm.

As these specimens were not found in connection with the skull MGPT-PU 13881/1-2 and because we are unable to find diagnostic characters, we assign MGPT-PU 13881/3 and MGPT-PU 13881/4 to *Odontoceti Incertae sedis*.

Discussion. The teeth from MGPT-PU 13881/3-4 were not described by Portis [8]. These teeth lack diagnostic characteristics, and for this reason, we assign them to *Odontoceti Incertae sedis*. In reality, the teeth originally described and discussed in ref. [8] are lost and cannot be studied. Based on the original illustrations (reproduced in Figure 2), it is evident that these teeth lack diagnostic characteristics at the family level. For this reason, we declare *Tursiops miocaenus* a *nomen dubium*.

Eurhinodelphinidae Abel, 1901 [29]

Remarks. Species in the extinct family Eurhinodelphinidae have long rostra and skulls with a peculiar derived morphology [27]. The main characters are (1) a comparatively very long rostrum that shows a great enlargement of the apical part of the premaxillae that constitute approximately one-third of the rostrum length; (2) the mandible is much shorter than the rostrum extending anteriorly approximately at the same level of the maxilla; (3) and a transversely compressed pterygoid-palatine region that is related to the ventral development of the vomer [30]. It must be stated that the derived character that was primarily thought to define the family is the extreme elongation of the edentulous premaxillary part of the rostrum, which can only be observed in *Eurhinodelphis*, *Schizodelphis*, and *Ziphiodelphis* [19].

The eurhinodelphinid skull architecture is squalodont-like but more specialized, as the posterior process of the periotic is small and only very loosely articulated with the squamosal, a condition that foresees the Delphinida morphology where the process is not articulated as being totally surrounded by ligaments that maintain it in situ. In the Eurhinodelphinidae, it likely made contact with the skull only and was not articulated to it as it is in the Platanistoidea or the Physeterida. The latter groups still retain a pterygoid lateral lamina [30]. Muizon [30] suggested that eurhinodelphinids are related to another extinct group, the long-beaked Eoplatanistidae (Early Miocene), and that both can be placed in the superfamily Eurhinodelphinoidea. Muizon [30] placed eurhinodelphinoids as a sister taxon to the large group including Delphinoidea, although the relationships are still not certain [27].

Eurhinodelphinoid characteristics observed in MGPT-PU 13881/1-2 include the following: (i) The involucrum is indented; (ii) the anterior process of the periotic bears two articular facets for the tympanic bulla (one is the epitubary fossa) [18]. In addition to these, there are other diagnostic characteristics that are missing in the present specimen due to taphonomic processes (i.e., the extreme elongation of the edentulous premaxillary part of the rostrum, the long rostrum with the maxillary-premaxillary suture located in a lateral sulcus, and a thick postglenoid process). Furthermore, a periotic with a round pars cochlearis and a smooth anterior surface is found in many specimens of the Eurhinodelphinidae family. Finally, in the Eurhinodelphinidae, the size of the pars cochlearis and that of the anterior process are comparable, showing a 1:1 ratio [19,31], a characteristic also found in MGPT-PU 13881/1-2.

Ziphiodelphis Dal Piaz, 1908 [32]

Ziphiodelphis sigmoideus Pilleri, 1985 [9]

Holotype. MGP-PD 26396–26403 from the Upper Aquitanian-Lower Burdigalian of the Belluno area.

Described material. Partial skull (MGPT-PU 13881/1), fragment of left mandible (MGPT-PU 13881/1), left tympanic bulla (MGPT-PU 13881/2), right tympanic bulla (MGPT-PU 13881/2), right periotic (MGPT-PU 13881/2), and left periotic (MGPT-PU 13906) (Table 1). The specimen MGPT-PU 13881/1 underwent additional preparation as, in its original condition, most of the skull surface was covered by the matrix (Figure S1 in Supplementary Material).

Remarks. The attribution of MGPT-PU 13881/1-2 to *Ziphiodelphis sigmoideus* is supported by several characteristics, including the overall shape of the anterior process of

the periotic, the size and shape of the lateral tuberosity of the periotic that is elongated and rounded, and a robust zygomatic process of the squamosal that shows a globular expansion located anterodorsally and a small facet for the articulation with the zygomatic bone more ventrally. The zygomatic process of the squamosal is thus squared in the lateral view, showing a morphological pattern that is exclusive to *Ziphiodelphis sigmoideus*.

Locality and horizon. The specimen MGPT-PU 13881/1-2 was likely found in the latest part of the 19th century in the PdC Formation in Rosignano Monferrato (Alessandria Province), Piedmont, NW Italy (Figure 1).

The sedimentary rocks of this region (the Monferrato area) are divided into two stratigraphic sequences resulting from two different tectonostratigraphic domains. In particular, the succession of the eastern Monferrato (Oligocene and Lower Miocene) consists of terrigenous sediments of variable depth, which are covered by shallow-water carbonates [5]. The sediments show conspicuous and nuanced lateral variations that make it difficult to refer to them as a single lithostratigraphic unit. The sedimentary sequence of eastern Monferrato includes several units among which the Pietra da Cantoni (PdC) is located at the top. The PdC consists of clastic rocks, typical of a relatively shallow marine depositional environment and influenced by waves; the sediments are indicative of a paleobiotope (developed in a warm tropical sea) located in an outer subsiding carbonate platform and slope, showing a transgressive trend and a deepening of the basin from east to west [2,3,24] and literature therein).

The PdC is divided into two sequences. The oldest one, (Aquitanian-Lower Burdigalian, Zone N5-N6) [5] is exposed exclusively in the Rosignano Monferrato area; it consists solely of carbonate rocks typical of the outer shelf, including bioclastic wackestone and packstone with scattered rhodoliths [33]. The boundary with the overlying sequence is an erosional slope surface. The second sequence is, in turn, subdivided into two units. The lower unit consists of coarse bioclastic limestone from a shallow marine environment and the upper one consists of marly packstones and marls deposited in a deeper environment [33].

Micropaleontological studies of the second sequence have shown a planktonic foraminiferan assemblage that allows one to refer to these sediments as the Burdigalian p.p.-Langhian p.p. (Biozone N7b-N8 corresponding to a range between *c.* 17.3 and *c.* 14.8 Ma; NI) [34]. In particular, at Rosignano Monferrato, the lower zone has a characteristic assemblage with benthic foraminiferans typical of the circalittoral to epibatial zone [35], which indicates a vegetated and well-oxygenated shelf substrate. The upper zone, on the other hand, has been interpreted as a foramol carbonate platform (typical of temperate seas) and an internal rhodalgal subtype, with a hard substrate and high hydrodynamic energy [36].

Unfortunately, the exact stratigraphic location of the fossil within the PdC is unknown; therefore, since it cannot be referenced to any of the biozones mentioned above, it is generically assigned to the late Burdigalian (approximately 16–19 million years ago) [3] (Figure 1).

4. Description of the Skull MGPT-PU 13881/1-2, MGPT-PU 13906

4.1. Skull

Overall, the elongated skull (MGPT-PU 13881/1) is trapezoid in shape, with an antero-posterior length of *c.* 320 mm (from the occipital condyle to the broken end of the rostrum) and a maximum width of *c.* 200 mm measured at the height of the anterior portion of the basioccipital (Figure 4). The rostrum is moderately well preserved and includes both the maxillae and the right dentary; the anterior end of the maxillae, premaxillae, vomer, nasals, and the left dentary are missing. There is no evidence of the presence of teeth and alveoli. The lack of the supraoccipital allows the observation of the skull base, including basioccipital, basisphenoid, and presphenoid, and periotic, tympanic bullae, and occipital condyles, which are present together with parts of the exoccipital including the paroccipital

processes. In the lateral view, it is possible to describe the squamosal, the temporal fossa, and part of the frontal. Measurements are provided in Tables 4 and 5.

Table 4. Measurements in mm of 13881/1: Skull and partial mandible.

Character	Length	Width	Transverse Diameter	Height/Thickness
partial skull	320	200		
partial basisphenoid-basioccipital	80	43		
hypoglossal canal			2	
hiatus cranicus			18	
foramen ovale			5	
left and right dorsal carotid foramen			2	
partial right occipital condyle			30	
hiatus cranicus			10	
basioccipital crest at the base	67	25		36
basioccipital crest at the apex	67	25		20
temporal fossa	44	26		
rostrum at the base	180	67		65
rostrum at the apex	180	67		25
antorbital notch				15
mesorostral groove at the base		23		20
mesorostral groove at the apex		14		20
right mandible at the base	240	55		35
right mandible at the apex	240	25		15
mandibular condyle			20	
partial left mandible	110	25		

Table 5. Measurements in mm of 13881/2, 13906: Tympanic bullae and Periotics.

Character	Length	Width	Transverse Diameter
right tympanic bulla	35	25	
left tympanic bulla	35	25	
tympanic cavity of right bulla		13	
tympanic cavity of left bulla		8	
right periotic	35	25	
anterior process of right periotic	15		
posterior process of right periotic	15		
internal acoustic meatus of right periotic			9
dorsal opening of the vestibular aqueduct of right periotic			5
cochlear window of right periotic			2
vestibular window of right periotic			2
right periotic: fossa for malleus			2.6
lateral tuberosity of right periotic			4
left periotic	28.6	20	
anterior process of left periotic	15		
internal acoustic meatus of left periotic			8
dorsal opening of the vestibular aqueduct of left periotic			4.7
cochlear window of left periotic			2.5
vestibular window of left periotic			2
left periotic: fossa for malleus			3
lateral tuberosity of left periotic			5.8

4.2. Rostrum

In the dorsal view, the incomplete rostrum is triangular with an anterior angle of *c.* 60 degrees (Figure 4). It consists of complete maxillae and the right dentary. Maxillae and dentary are well aligned with a constant angle with respect to the axis of the rostrum. In the preserved portions of both the maxillae and dentary, there are no alveoli or teeth. The

length of the rostrum, although truncated, corresponds to more than half of the skull, and its dimensional relationships resulted in a very elongated and regular shape, suggesting that the rostrum was rather narrow in origin.

It is not possible to determine the precise shape of the cross-section orthogonal to the axis of the rostrum since both the premaxillae and the left dentary are missing; however, judging from what is preserved, the outline of the lateral surfaces is rounded. The connection with the frontal shows, in dorsal view, an evident antorbital notch with an acute angle approximately 15 mm deep.

The premaxillae are not preserved with the exception of a small residual fragment, which can be observed at the upper margin of the right maxilla, very close to the frontal.

The maxilla constitutes most of what is preserved of the rostrum. The right maxilla is more complete than the left one, which lacks the posterior part; the anterior border is jagged as the anterior portion of the rostrum is broken off and missing. Instead, the antorbital process, the antorbital notch, the maxillary crest, the mesorostral groove, and the right choana are complete.

In the dorsal view, on the upper part towards the center of the rostrum, there are two linear and shallow furrows (one more evident on the left side) that separate the external surface from the rostral surface and run to the anterior end of the preserved maxilla. These furrows converge toward the longitudinal axis of the rostrum and delimit the mesorostral groove (Table 2). These lines mark the boundary between the maxilla and premaxilla. At the base of the mesorostral groove is the suboval depression of the right choana, delimited on the right by the curved wall of the maxilla. At the left base of the rostrum, the maxilla is curved and rises, and part of it is broken and subdivided into small fragments.

In the ventral view, the medial part of the left maxilla includes the palatine process (hard palate) (Figure 4C,D). Approximately at mid-length, two slightly oblique and symmetrical furrows are developed from the medial border and diverge posteriorly, forming an acute angle of approximately thirty degrees. This structure corresponds to the palatine groove that separates the palatine process from the anterior border of the palatine. The left palatine process is slightly arched in the cross-section.

The posterior portion of the right maxilla is superimposed on the frontal forming a small facial fossa. The posterior border of the maxilla runs obliquely from the antorbital notch towards the center of the skull.

Assuming that the suture line visible on the left maxilla in the ventral view corresponds to the median axis of the rostrum, it is possible to infer the lateral size of the rostrum at the height of the condyle of the right mandibular ramus. The measurement of the distance between the outermost part of the condyle and the longitudinal axis is 83 mm. Therefore, the size (transversal diameter) of the rostrum originally had to be double at this point, therefore measuring approximately 166 mm. This hypothesis was also found unquantified in one of the previously published studies [1] in the drawing with the reconstruction of the skull.

The vomer is observed in the dorsal view within the mesorostral groove. Its dorsal surface is dorsally concave, and it is round in the transverse section.

4.3. Frontal

The right frontal eminence is partially covered by the posterior portion of the maxilla. The orbital rim is evident in the dorsal view. The external border of the frontal (corresponding to the orbital rim) is laterally concave and anteromedially oriented. In the lateral view, the orbit appears anteriorly damaged (Figure 5). Only the postorbital process is well preserved and appears as a massive and posteriorly curved elongated structure with a rounded posterior end. It is articulated with the anterior end of the zygomatic process of the squamosal.

4.4. Squamosal

On the right side, the squamosal is well preserved. It forms the concave posterior wall of the temporal fossa and shows a massive zygomatic process pointing towards the supraorbital process of the frontal. Mid-ventrally, it shows a massive basal extension forming the glenoid fossa for the jaw joint. The zygomatic process is in contact with the postorbital process of the frontal. In the dorsal view, it projects laterally to the parietal. In the dorsal view, the zygomatic process of the squamosal extends anteriorly with an angle of 40 degrees with respect to the longitudinal axis of the skull; its rounded anterior end makes contact with the postorbital process of the frontal, leaving the temporal fossa on its left, which is 26 mm wide and 44 mm long.

The supramastoid crest is low and projects dorsally and laterally; it forms the dorsal border of the zygomatic process of the squamosal and is linked to the posterior termination of the temporal crest. In the posterior portion of the zygomatic process of the squamosal, ventrally to the supramastoid crest, there is an elongated, triangular fossa for the sternocephalic muscle (Figure 5). In the lateral view, the suture with the parietal and the contact with the alisphenoid are not recognizable.

4.5. Mandible

Two mandibular fragments are present. The left mandibular ramus (MGPT-PU 13881/1) was represented in a photographic plate in ref. [6] in which it was part of the main block including the skull and the right mandibular ramus. After the recent preparation, the left mandibular ramus consists of an isolated fragment (Figure 6A,B). It is 110 mm in length, 25 mm in width at its widest point, and 18 mm in width towards the extremity, where the bone with the characteristic reddish-brown porcelain appearance is fully visible. There are no teeth or alveoli in this mandibular fragment. The rest of the fragment consists of a cast of the internal canal made of whitish calcareous sediment. The presence of bone remains allows the reconstruction of the medial surface of the mandibular ramus, which is medially convex. Based on a previously published photographic plate [6], it seems that this fragment corresponds to the terminal part of the mandibular ramus still in its original position with respect to the maxilla.

The larger fragment is represented by the long, narrow, and tapered right mandibular ramus (Figure 6C,D). Its length is *c.* 240 mm and the width is 55 mm in the uppermost part near the skull and *c.* 25 mm at the tip. Its thickness at its base is approximately 35 mm, reaching approximately 15 mm (Figure 6) at the end. The anterior end is broken and, therefore, the total length cannot be determined. In the posterior part, it widens slightly, and the inner border curves and curls giving rise to the mandibular condyle. In the posterior portion, well-preserved parts of the original bone are exposed, recognizable by their porcelain appearance and reddish color, which is different from that of the surrounding matrix. The condyle, the angular process, the masseteric line, and likely the coronoid process are hidden under the frontal bone and cannot be described.

The mandibular condyle is posteriorly protruding, especially in the ventral view; in the lateral view, it is covered by the squamosal. The presence of the jugal bone was previously reported in close proximity to the mandibular ramus [1] but the recent preparation of the specimen revealed that it is absent. The bony structure that was previously identified as the jugal in ref. [1] is rectangular in shape and is located dorsally to the condyle and below the squamosal; it is separated from both the mandible and the squamosal by deep grooves. Based on its morphology, it cannot be safely attributed to the jugal and may represent part of the squamosal.

In the ventral view, the condyle is posteriorly rounded with a diameter of approximately 20 mm; it is bent ventrally and slightly extended along the anteroposterior axis of the mandibular ramus. In the ventral view, however, the condyle lies on the squamosal for approximately 5 mm, in correspondence with the mandibular fossa; in the right lateral view, the squamosal overlaps the mandibular ramus for approximately 20 mm.

The coronoid process is crushed under the skull; small fragments of it are visible between the mandibular ramus and the ventral surface of the skull. The angular process is missing; only a cast of it can be observed in the mandible in the lateral view. Assuming that the cast represents the correct morphology of the angular process, it shows a rounded posteroventral edge and protrudes posteriorly to a lesser extent compared to the mandibular condyle (Figure 6).

4.6. Basicranium

In the dorsal view (Figure 7), parts of the skull base are visible on the left side of the specimen, delimited on the right by what remains of the parietal. The basisphenoid shows a shallow and concave sella turcica. The basioccipital and the right parietal are partially present. The total length of the basisphenoid–basioccipital complex is approximately 80 mm.

In the posterior part of the basioccipital, in the paraxial position on the right side, there is the hypoglossal canal with a sub-oval shape (maximum diameter = 2 mm) for the passage of the XII cranial nerve. The right hiatus cranicus is located between the basioccipital and the parietal; it is subcircular in outline and shows a maximum transverse diameter of 18 mm. It tilts anteriorly towards the temporal fossa. Next to the hiatus cranicus, there is a tuberosity (tentorium) and, immediately posteriorly to the tentorium, it is possible to observe the foramen ovale (maximum diameter = 5 mm) for the passage of the mandibular branch of the trigeminal (V) cranial nerve. The maximum distance between the two tuberosities of the tentorium is approximately 43 mm. Each tuberosity is in line, orthogonally to the axis of the skull, with another larger and protruding tuberosity placed on the outer surface of the fragment; the latter is flanked posteriorly by a partial left hiatus cranicus (maximum transverse diameter = 18 mm) and anteriorly by the contralateral foramen ovale. In the central part of the basisphenoid, on the two sides of the sella turcica, there are two carotid dorsal foramina with diameters of 2 mm. Posterior to the left maxilla, the suboval concavity opens (approximately 1 cm in maximum depth) of the right choana, which shows a maximum diameter of 30 mm. Posteriorly, another concavity (maximum transverse diameter = 34 mm) is adjacent to the sella turcica on the left side, likely corresponding to the ventral prominence of the pons. At the posterior end of the skull, only part of the right occipital condyle is preserved, which shows a maximum transverse diameter of 30 mm (Figure 8).

In the ventral view, part of the right occipital condyle, the massive crest of the basioccipital, and the opening of the right hiatus cranicus are clearly visible. The basioccipital crest is 67 mm in length, 25 mm in width, and 36 mm in height at the posterior end, and 20 mm in height at the anterior end. It is oriented along the main axis with a slight inclination forward and to the right. It appears as a well-developed, sub-cylindrical structure emerging from the base of the skull, where it is narrower, with a rounded posterior end and a more tapered anterior end. It is anchored to the basisphenoid and basioccipital and overhangs the right side, forming a long and deep hollow under the basioccipital. In the ventral view, in the angle between the occipital condyle and the basioccipital crest, there is a hollow corresponding to the peribullary sinus (maximum anteroposterior diameter = c. 24 mm) from which the right tympanoperiotic complex (periotic and bulla) was dissected and detached from the skull [1].

In the dorsal view, the parietal is a thin, elongated, and curved bone that forms part of a basin with a diameter of approximately 54 mm, whose floor is connected to the basioccipital. Its sub-vertical part rises approximately 30 mm from the basioccipital and above the squamosal on the right side. In the dorsal view, the parietal is thin and curves upwards, converging towards the longitudinal axis of the skull medially close to the choana.

The suture between the basioccipital and the basisphenoid is fused, while a sinuous suture is noted between the alisphenoid, the parietal, and the squamosal, which continues up to the foramen ovale.

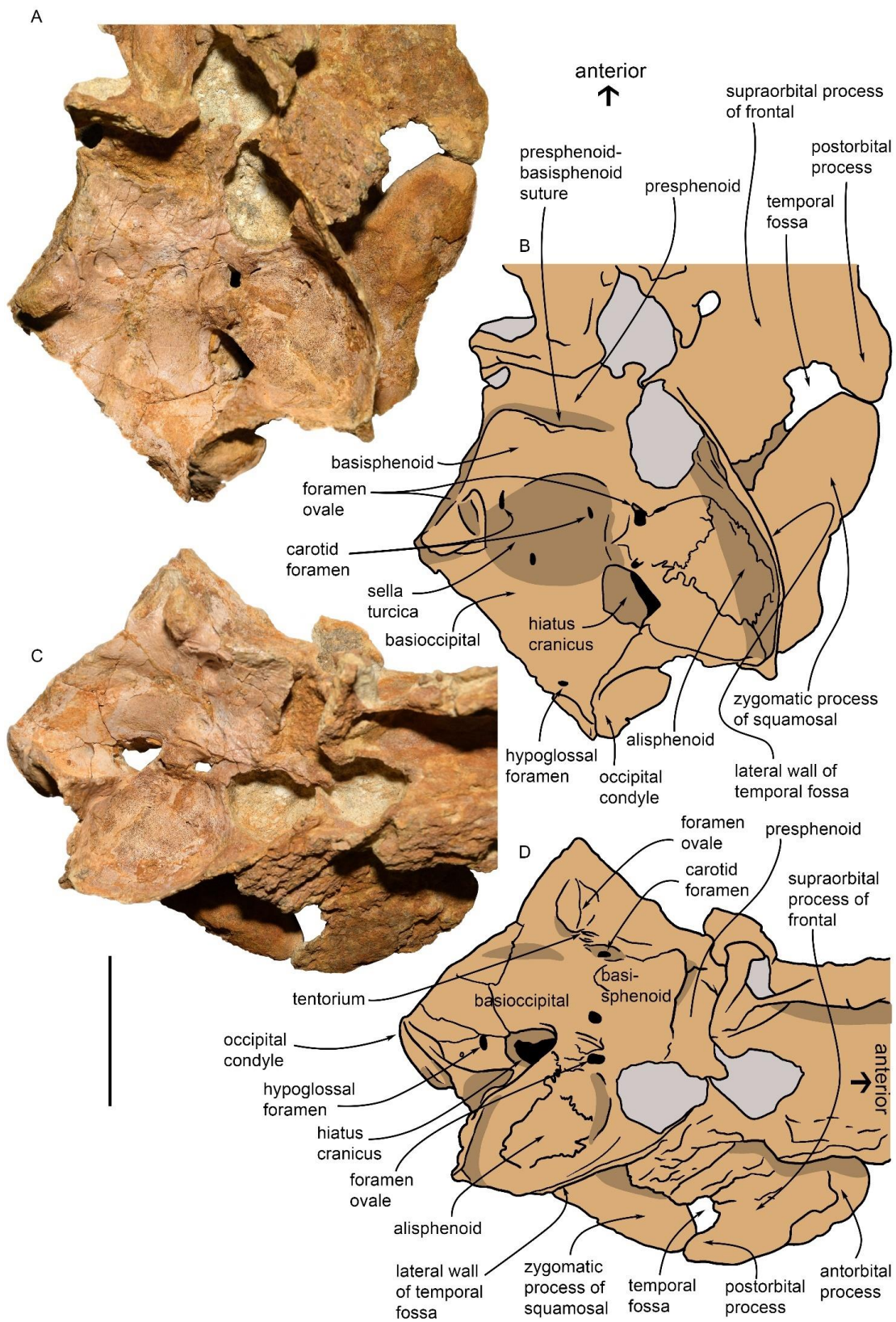


Figure 7. Basicranium of MGPT-PU 13881/1. (A) Photographic representation of the basicranium in dorsal view. (B) Anatomical interpretation of (A). (C) Photographic representation of the basicranium in right dorsolateral view. (D) Anatomical interpretation of (C). Scale bar equals 5 cm.

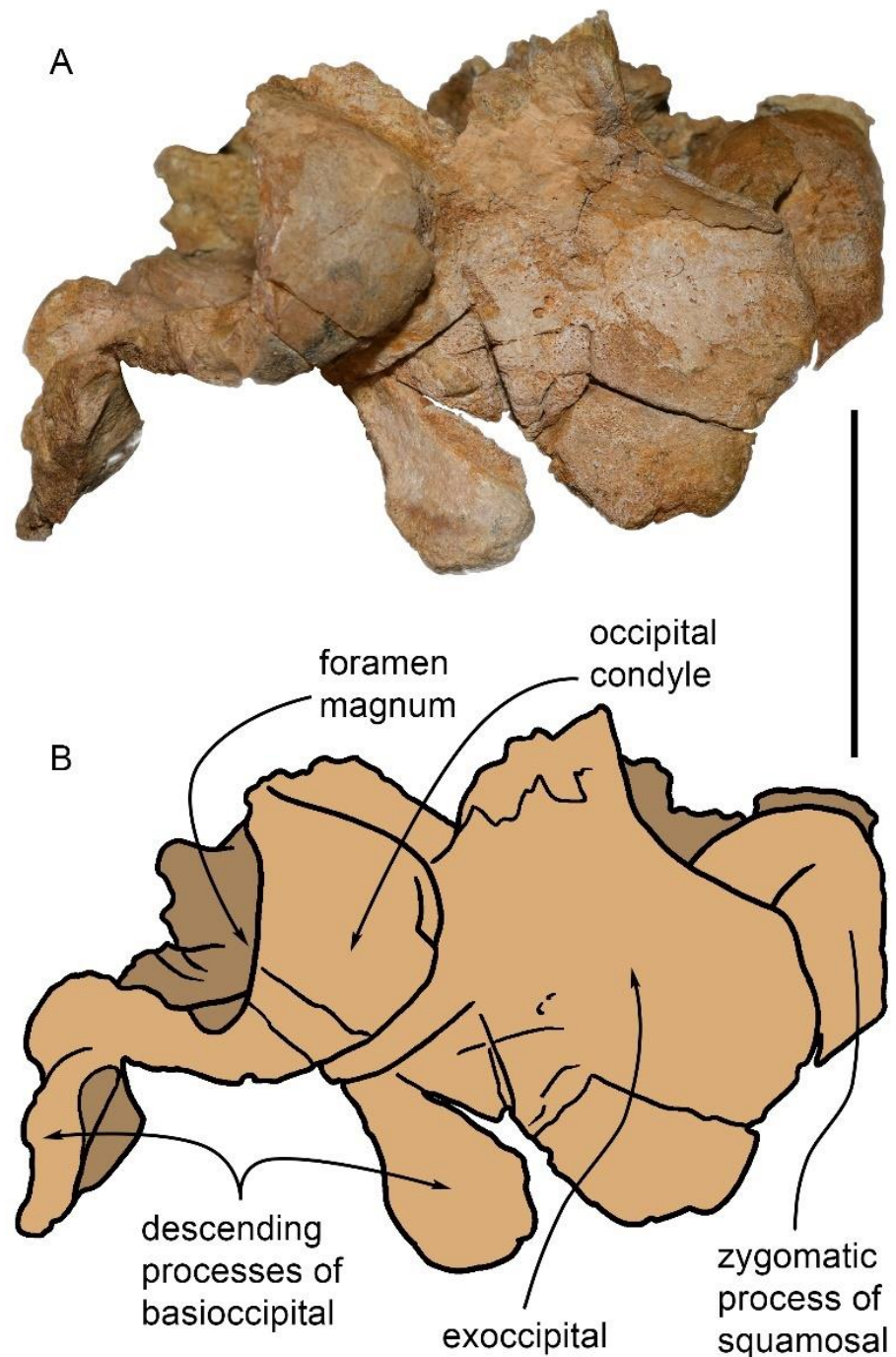


Figure 8. Partial skull MGPT-PU 13881/1 in posterior view. (A) Photographic representation. (B) Anatomical interpretation of (A). Scale bar equals 5 cm.

4.7. Tympanoperiotic Complex: Overview

The tympanoperiotic complex is formed by the periotic and the tympanic bulla. In the odontocetes, the complex is suspended within the peribullary sinus of the squamosal; the whole complex is located at the base of the squamosal near the craniomandibular joint. The right tympanoperiotic complex was separated from the skull in 1994; in addition, the isolated left tympanic bulla is present. Measurements are provided in Table 5.

In the examined specimen, the periotic bone and the tympanic bulla are two separate structures. Both are very similar in size (length of 35 mm and width of 25 mm), and the 1:1 dimensional ratio is a typical feature of odontocetes [37].

4.8. Tympanic Bulla

The right bulla is elongated, with an elliptic outline and a length-to-width ratio of 1.4 (Figure 9A–E). It consists of thin bone tissue with a pinkish porcelain appearance. The dorsal view shows a large tympanic cavity, approximately 13 mm wide, which extends longitudinally for the entire length of the bulla. Closely to the posterior end, the intact involucrum projects towards the inside of the cavity (Figures 9 and 10). Most of the cavity is filled with a sedimentary matrix. The structure is not complete since the posterior process, sigmoid process, accessory ossicle, and anterior pedicle are missing. The absence of the posterior process makes the tympanic opening visible; in the posterior border of the bulla, the elliptical foramen is present, rounded, and bordered by a thin crest.

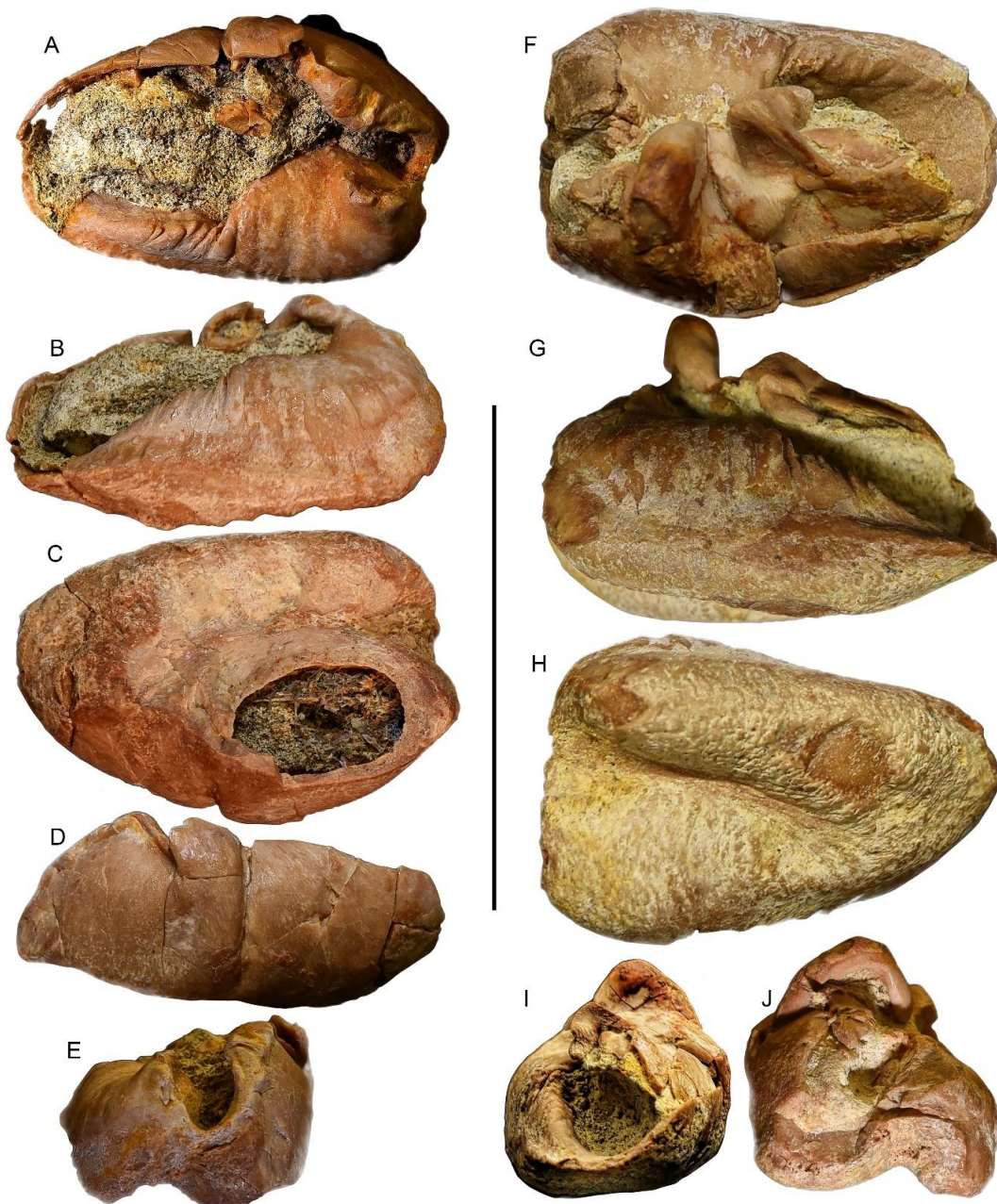


Figure 9. Tympanic bullae. (A–E) Specimen MGPT-PU 13881/2. (A) Dorsal view. (B) Medial view. (C) Ventral view. (D) Lateral view. (E) Posterior view. (F–J) Specimen MGPT-PU 13906. (F) Dorsal view. (G) Medial view. (H) Ventral view. (I) Anterior view. (J) Posterior view. Scale bar equals 5 cm.

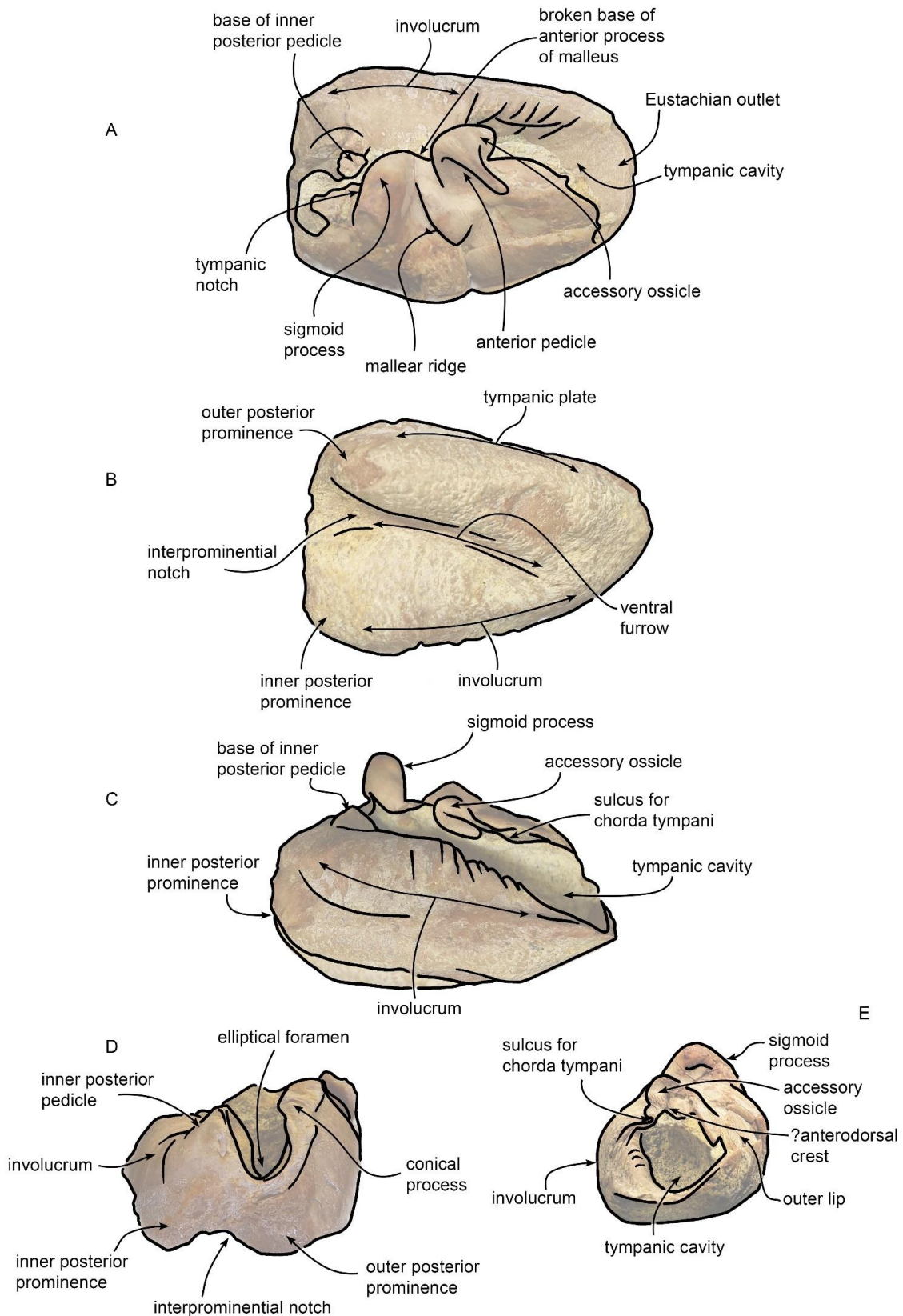


Figure 10. Anatomical interpretation of characters observed in the tympanic bullae MGPT-PU 13881/2 and 13906. Not to scale. (A) dorsal view. (B) ventral view. (C) medial view. (D), posterior view. (E) anterior view.

In the lateral view, the base of the sigmoid process can be observed. In the ventral view, the posterior portion of the bulla shows an asymmetrical bilobated aspect by showing inner and outer posterior prominences; the inner posterior prominence is larger and more prominent than the outer one. The two lobes are separated by the interprominential notch and the median furrow that extends beyond the middle part of the bulla, curving towards the left lobe, which presents a circular break.

Differing from the right bulla, the left bulla is characterized by greater integrity of the structure (Figure 9F–J). The size, porcelain appearance, and morphology are similar to those of the right bulla. In the dorsal view, the tympanic cavity is tighter than the other (a width of approximately 8 mm) since the conical process, sigmoid process, anterior pedicle, and accessory ossicle are present on the left edge of the bulla. The posterior process is absent.

The conical process resembles a slightly prominent and rounded crest. The sigmoid process, with a massive irregular tubular appearance, has swelling at the base that overhangs the conical process below. It emerges laterally with a sinuous appearance, becoming gradually more protruding and curving; it enters the tympanic cavity. In the lateral view, the tympanic notch between the sigmoid and conical process can be seen. From this process, the anterodorsal crest departs upwards.

The accessory ossicle and anterior pedicle appear above the sigmoid process as slightly protruding folds that occlude the tympanic cavity. The anterior pedicle overlaps the accessory ossicle. In the ventral view, the two asymmetrical lobes of the inner and outer posterior prominences are clearly observed with an evident interprominential notch and a deep median furrow that extends beyond the middle of the bulla, branching off at the extremity and curving slightly towards the outer posterior prominence.

4.9. Periotic

The right periotic, originally present in situ in the fossil, was mechanically separated from the cranium in 1994 (Figures 11 and 12). The periotic shows a translucent pinkish appearance and has an irregular shape. It consists of a globular central body, corresponding to the cochlear portion, and two wings, representing the anterior and posterior processes, which are separated from the central body by an angle of approximately 120 degrees. The maximum length of the periotic is approximately 35 mm, the two processes have the same size with a length of 15 mm, and the cochlear portion has a diameter of approximately 18 mm. The size of the periotic is equivalent to that of the tympanic bulla. Calcareous sediment fills the floor of the periotic foramina.

In the medial view, the dorsal border of the periotic shows a dorsally concave outline with the anterior process forming an anterior convexity. The anterior process is triangular in the medial view with a pointed anterior end. The suprameatal area is flat. The internal acoustic meatus is pear-shaped and shows an anterodorsal endocranial opening of the facial canal and a ventral dorsal vestibular area. The endocranial opening of the facial canal is anteroposteriorly elongated and dorsoventrally narrow; a short fissure departs from its anterodorsal border. It is separated from the dorsal vestibular area by a shallow transverse crest that does not reach the rim of the internal acoustic meatus. The dorsal vestibular area is partially filled by sediment. However, a large oval area (likely corresponding to part of the foramen singular and the anterior-most portion of the spiral cribriform tract) and a smaller circular area (likely corresponding to the posterior-most portion of the spiral cribriform tract). Posteriorly to the internal acoustic meatus, the aperture for the vestibular aqueduct (endolymphatic duct) is dorsoventrally elongated and anteroposteriorly narrow; the aperture for the cochlear aqueduct (perilymphatic duct) is well separated from the endolymphatic duct by a thick crest and shows a wide and circular outline. A median promontorial groove is evident, especially in the posterior view.

The round window opens shortly ventrally from the perilymphatic duct and shows a continuously curved ventral border with a ventral convexity; the dorsal border is also ventrally convex and continuously curved. Acute corners separate the ventral and the dorsal borders.

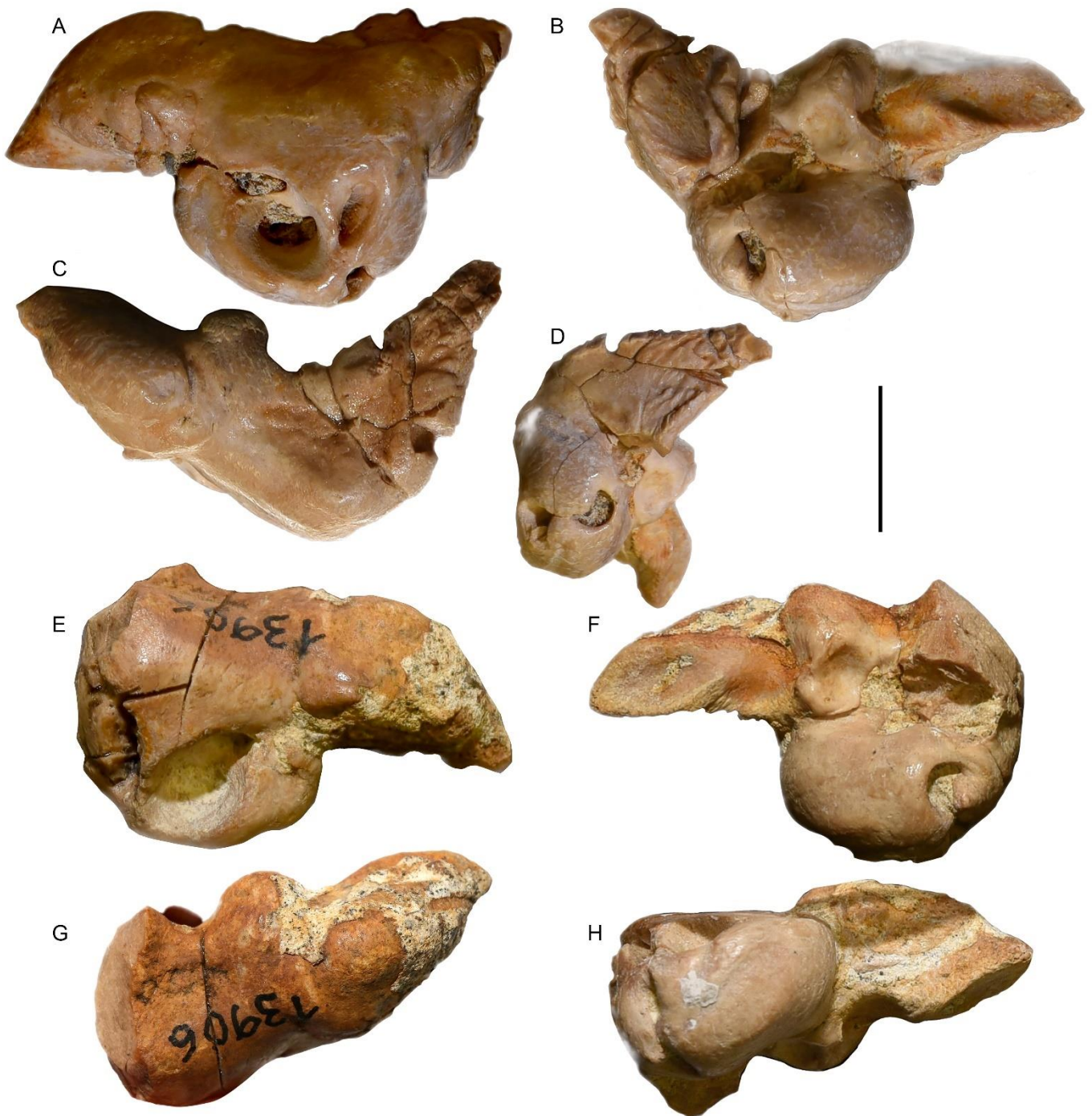


Figure 11. Periotics. (A–D) MGPT-PU 13881/2. (A) Medial view. (B) Lateroventral view. (C) Dorsal view. (D) Posterior view. (E–H) MGPT-PU 13906. (E) Medial view. (F) Lateral view. (G) Dorsal view. (H) Ventral view. Scale bar equals 2 cm.

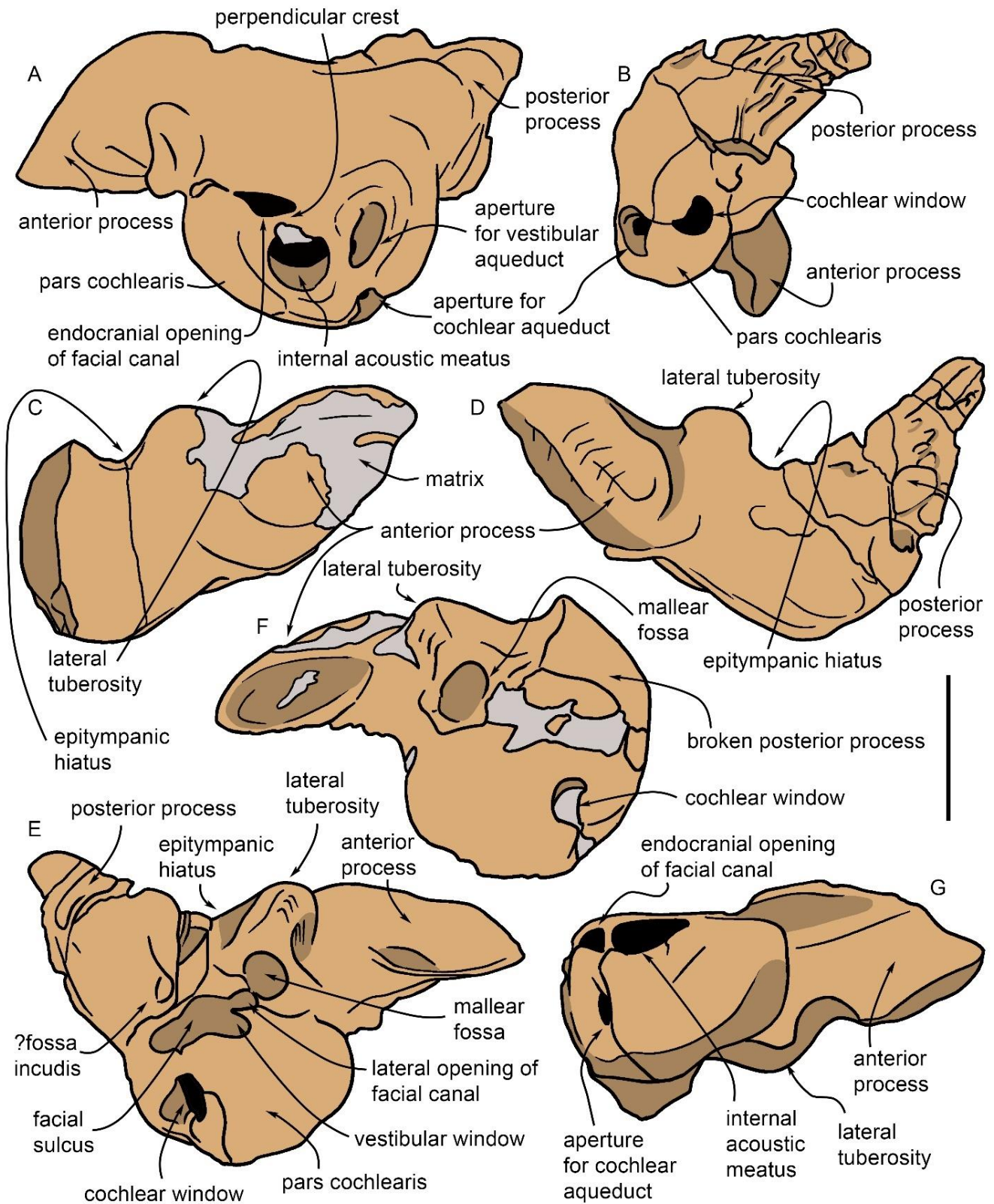


Figure 12. Anatomical interpretation of periotic morphology. (A) Medial view. (B) Posterior view. (C) Dorsal view of MGPT-PU 13906. (D) Dorsal view of MGPT-PU 13881/2. (E) Lateral view of MGPT-PU 13881/2. (F) Lateral view of MGPT-PU 13906. (G) Ventral view of MGPT-PU 13906. Scale bar equals 2 cm.

In the dorsal view, the periotic shows an evident and inflated anterior process that has a vaguely triangular shape and externally convex borders, a posteriorly tapering posterior process that has a broadly triangular shape, and an almost rectangular central portion. A notable, elliptical, and protruding lateral tuberosity is observed just behind the posterolateral corner of the anterior process; the epitympanic hiatus is reduced to a triangular space included between the protruding lateral tuberosity and the lateral border of the posterior process.

In the lateral view, the oval window is partly filled by sediment; its ventral and anterior outlines are continuously curved. Furthermore, the lateral opening of the facial canal is filled with sediment and its outline cannot be clearly observed. A crest separates the area where the oval window opens from the broad and elliptic fossa for the stapedial muscle. Unfortunately, the area comprised between the facial crest of the periotic and the lateral tuberosity, in the lateral view, is broken and inadequately preserved. In the medioventral view, the anterior process shows a concave ventral surface developed posteriorly to the triangular and pointed anterior end.

Moving towards the end of the anterior process, two elongated depressions can be recognized that are separated from each other by a ridge. The second of these depressions, which constitutes the terminal portion of the process, is the fovea epitubaria, with a pointed elliptical aspect at the end. The posterior process of the periotic, stockier than the anterior one, is furrowed by deep transverse incisions. Starting from the base, the first incision, in the upper position, corresponds to the stapedial muscle fossa. In the lower position, in correspondence with the epitympanic hiatus (i.e., the recess between the tuberosity and the posterior process), a deep incision with vertical walls can be observed, which can be interpreted as the tympanic sulcus, delimited on the right by the facial crest from which the facial sulcus follows. These incisions delimit the main body of the posterior process. The articular facet for the tympanic has a flattened, slightly expanded, and frayed edge with alternating ridges and small, barely distinguishable grooves parallel to the main axis of the process.

The left periotic is separated from the skull and is incomplete due to the loss of the posterior process (Figures 11 and 12). It shows a pinkish translucent appearance; it consists of the globular cochlear portion and, almost perpendicular to it, the anterior process.

The maximum length of the periotic is 28.6 mm; however, as seen in the right periotic, the anterior process shows a length of 15 mm, and the cochlear portion has a diameter of approximately 18 mm. The dimensions are comparable to those of its tympanic bulla and the contralateral periotic.

In the medial view, the four openings on the central body are less defined than in the right periotic. The left side of the cochlear portion appears to be extensively fractured but the dorsal opening of the cochlear aqueduct and the dorsal opening of the vestibular aqueduct (measuring approximately 4.7 mm) can be recognized. On the right side, it is possible to recognize the opening of the internal acoustic meatus (8 mm) showing the endocranial opening of the facial canal and the dorsal opening of the fallopian aqueduct.

4.10. Body Size Estimate

The resolved equation (1) (see Section 2.5) indicates that the occipital breadth of MGPT-PU 13881/1 is 47.01 mm. Therefore, Equation (2) described in the Section 2.5 provides an estimate of the body mass of MGPT-PU 13881/1 of 13.92 kg, which is consistent with the small size of the skull. Finally, equation (3) from the Materials and Methods section indicates a total skeletal length of *c.* 87 cm, which seems to underestimate the actual total length especially because this specimen had a long rostrum. We can confidently approximate a reasonable estimate of *c.* 1.5 m for the total length including *c.* 50 cm of the rostrum (missing in the specimen).

4.11. Paleoneurology

The 3D renderings of the photogrammetry-based reconstruction of the basicranium and virtual endocast are available from Morphosource (project: https://www.morphosource.org/concern/biological_specimens/000493295, accessed on 2 February 2023; virtual endocast: <http://n2t.net/ark:/87602/m4/493301>, accessed on 2 February 2023). Photogrammetry allowed a more detailed reconstruction of the tridimensional structures of the basicranium warranting a more detailed interpretation of the previously unrecognized anatomical characters (Figure 13). Orientation of the virtual endocast and basicranium within the skull is provided in Figure S2 (Supplementary Material) together with a schematic assessment of the lost portion of the endocast.

The 3D rendering of the basicranium shown in Figure 13 allows us to observe the presence of a chiasmatic groove slightly posterior to the anterior border of the basisphenoid. The chiasmatic groove is anteroposteriorly thick and its distal (lateral) end corresponds to part of the optic (II) cranial nerve that is directed laterally. A couple of orbital fissures are observed on the right side of the basicranium; these are large, ovoid openings on the ventrolateral surface of the skull that are separated by a thin, transverse crest. Posterior to the chiasmatic groove, a possible foramen rotundum (allowing the passage of the mandibular ramus of the trigeminal nerve: V_2) is observed as very close to the anterolateral edge of the tentorium.

The virtual endocast of MGPT-PU 13881/1 is shown in Figure 14 in ventral view. The virtual endocast represents only the temporal lobe and the ventral surface of the brain. The orientation of the endocast and an assessment of the number of lost portions of the endocast are shown in Figure S3 in Supplementary Material. The posterolateral edge of the anterior orbital fissure is continuous with the lateral edge of the optic chiasm. The optic chiasm is large and thick and shows a lateral termination corresponding to the optic (II) cranial nerve. The posterior orbital fissure is apparently isolated from the other neural structures. It is separated from the temporal lobe of the brain by a groove corresponding to the sylvian fissure, which separates the anterior edge of the temporal lobe from the other anterior cerebral structures. The temporal lobe is ovoid in shape and is separated from the other cerebral structures by the sylvian fissure anteriorly and dorsally. The temporal lobe is externally convex and shows a sharp anteroventral corner (Figure 15). Its maximum anteroposterior diameter is 61.9 mm and its maximum dorsoventral diameter is 37 mm. Judging from the dorsal view of the basicranium as shown in Figure 15A,B, the brain of MGPT-PU 13881/1 reaches its maximum transverse diameter posteriorly, at the level of the temporal lobe. The transverse diameter decreases as far as the anterior end of the brain is approached. The total volume of the temporal lobe is 55.88 cm³.

Very close to the anteroventral border of the temporal lobe, a large root for the trigeminal nerve ($V_{1,2,3}$) is observed. This root is approximately conical in shape, with the proximal portion more elongated and wider than the distal portion. The root of the trigeminal nerve is close to a position corresponding to the oval foramen. More medially, the two internal carotid structures are observed with a protruding, roundish hypophysis located between them. The distance between the hypophysis and the anterior border of the pons is 15.2 mm. As the total length of the cerebral hemisphere can be estimated as 124.2 mm (calculated as the distance from the foramen magnum and the anterior-most border of the basicranium), the hypothalamus quotient of MGPT-PU 13881/1 is 0.122.

Ventral and medial to the temporal lobe, at the lateral margin of the pons, the large root for the structures exiting through the hiatus cranicus is observed (Figures 14 and 15C–H). This root is approximately conical and has a maximum length of 22.6 mm and a maximum width of 24.3 mm. It includes the proximal portions of the cranial nerves VII-to-XI and some vascular structures of problematic interpretation. Posterior to the root for the structures entering the hiatus cranicus, the root of the XII cranial nerve is observed, matching the position of the hypoglossal foramen anterolateral to the occipital condyle.

All these roots emerge from the slightly convex ventral surface of the pons, which is an elongated neural structure extending from the hypophysis to the foramen magnum.

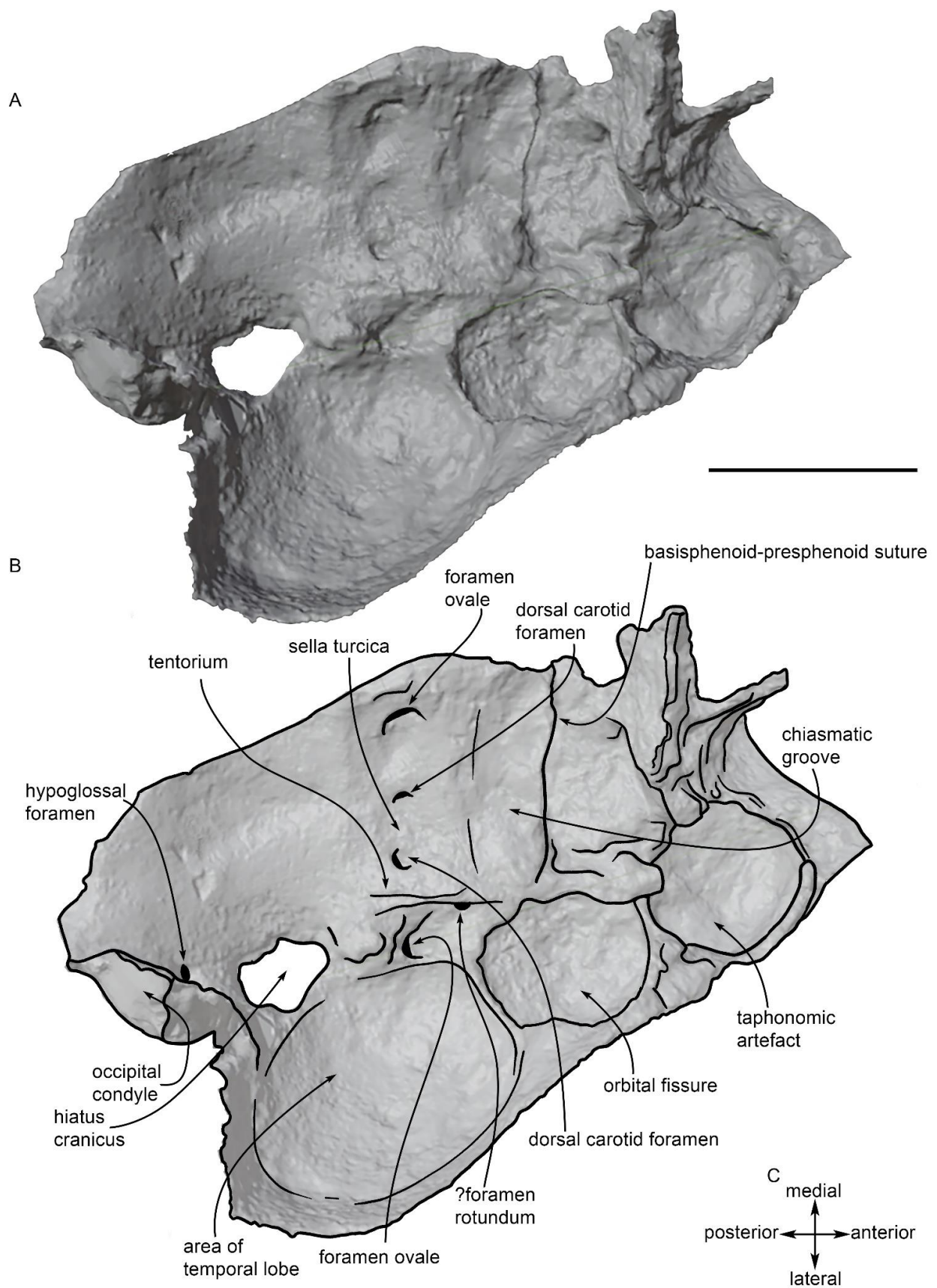


Figure 13. 3D virtual rendering of the basicranium of MGPT-PU 13881/1. (A) Software representation. (B) Anatomical interpretation. Scale bar equals 5 cm. (C) orientation of the basicranium.

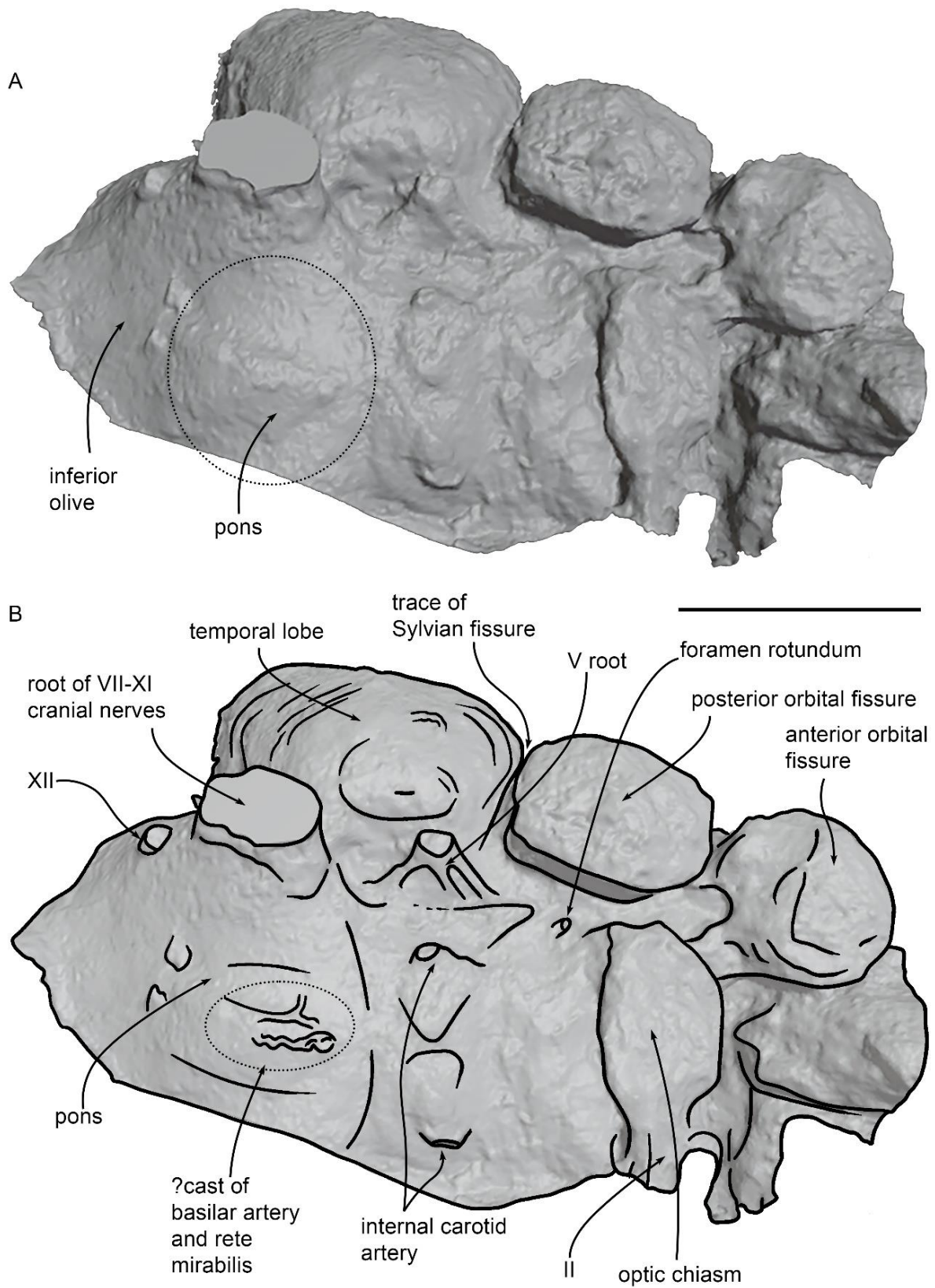


Figure 14. Virtual endocast of MGPT-PU 13881/1 showing the ventral surface of the brain. (A) Software representation. (B) Anatomical interpretation. Scale bar equals 5 cm.

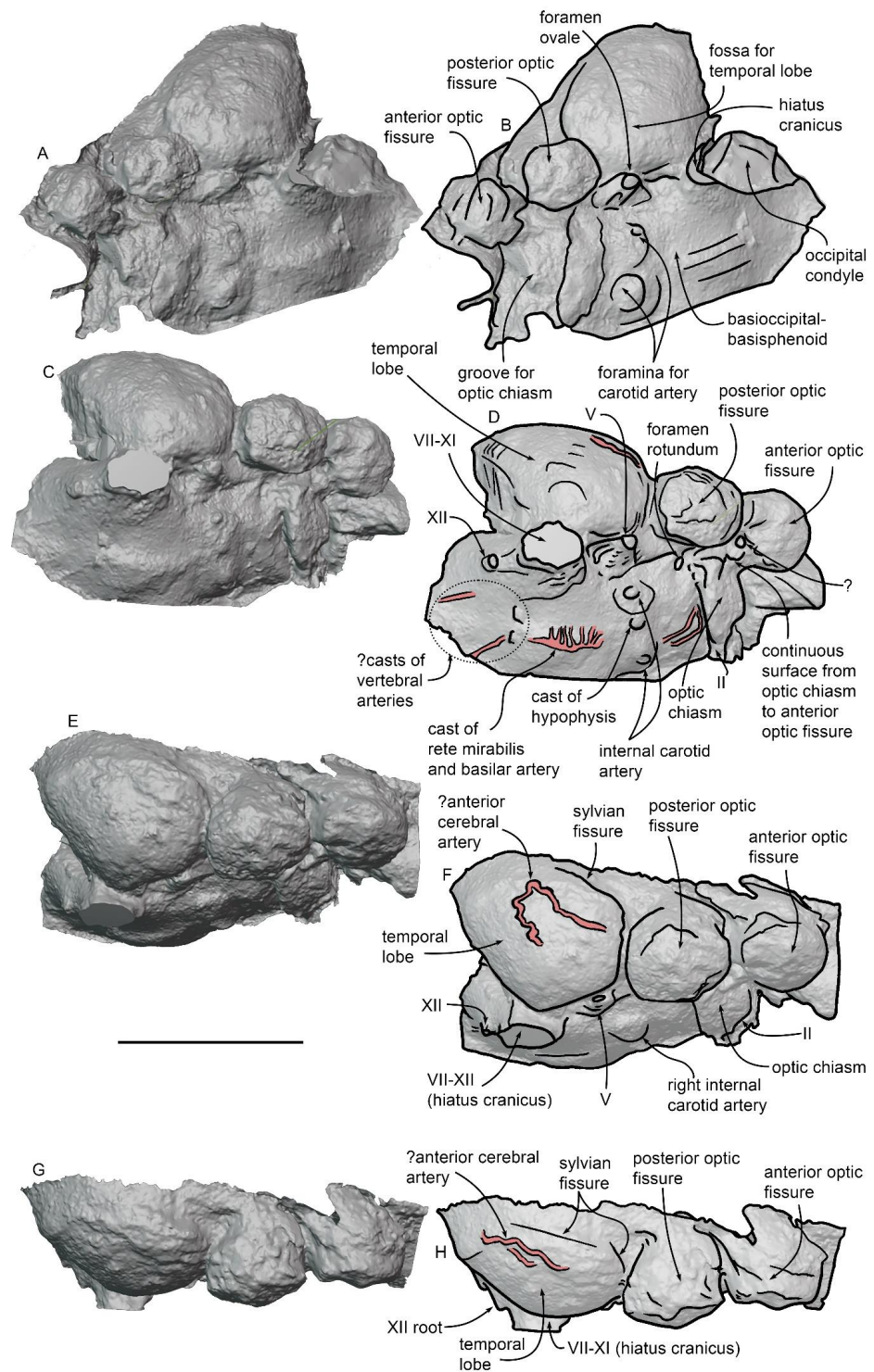


Figure 15. Virtual endocast of MGPT-PU 13881/1. (A) Software representation of the dorsolateral view of the basicranium. (B) Anatomical interpretation of (A). (C) Software representation of the ventral surface of the brain in the virtual endocast in ventral view. (D) Anatomical interpretation of (C). (E) Software representation of the ventral surface of the brain in the virtual endocast in ventrolateral view. (F) Anatomical interpretation of (E). (G) Software representation of the ventral surface of the brain in the virtual endocast in lateral view. (H) Anatomical interpretation of (G). Scale bar equals 5 cm.

Along the ventral surface of the pons, it is possible to observe the mold of a ramified structure that resembles the rete mirabilis, which is located posteriorly and ventrally in the brain of odontocete cetaceans [38] (Figure 15C–F). An underlying axial vessel is also observed in the position of the basilar artery from which the rete mirabilis is developed. Behind the posterior border of the pons, there are two paraxial structures; the left one of these structures is continuous with the mold of an elongated and narrow structure that occupies the position of the left vertebral artery [39]. We thus interpret these structures as the anterior-most portions of the right and left vertebral arteries that are recorded in the endocast only a few mm before merging into the basilar artery. The posterior portion of the right vertebral artery is located more posteriorly and laterally in the endocast (Figure 15C,D). The presence of simple vertebral arteries in MGPT-PU 13881/1 in contrast to the ramified and complex rete mirabilis observed in modern odontocetes (as synthesized in ref. [38]) suggests that the spinal rete mirabilis was not present in this eurhinodelphinid (see Discussion for further analysis of this point).

A sinuous and narrow structure is observed on the lateral side of the temporal lobe (Figure 15E–H). We suggest that this structure does not represent the spinal meningeal arteries complex that was previously described in the bottlenose dolphin [40] because such a complex is well developed along the posteroventral surface of the temporal lobe. Conversely, we find only a single sinuous structure developed in the center of the temporal lobe that does not show any sign of posterior development. We suggest that this structure does not represent the middle meningeal vessels previously described in dolphin endocasts [41,42] as its orientation is anteroposterior whilst the middle meningeal vessels are dorsoventrally oriented. We were unable to observe its origin and its further developments and ramification. Based on its position in the brain, we suggest that this structure may represent the anterior cerebral artery (Figure 15E–H).

5. Comparisons

5.1. Comparisons with Archaic Odontocete Families

Even though many of the diagnostic characteristics of Eurhinodelphinidae cannot be observed in MGPT-PU 13881/1-2 due to inadequate preservation, some characteristics of the periotic and tympanic bulla support its placement within this family. However, such a family-level placement can also be justified by a comparative analysis with other odontocete families.

The attribution of MGPT-PU 13881/1-2 to the Squalodontidae can be ruled out because the members of the family show a periotic with a long and narrow posterior process, a voluminous anterior process with poorly developed fovea epitubaria, and a well-developed anterior spine in the tympanic bulla. Moreover, squalodontids show a falciform process of the squamosal that is much more protruding, pointed, and inclined slightly downwards, with the zygomatic process not in contact with the postorbital process of the frontal.

Skull MGPT-PU 13881/1-2 differs from the Squalodelphinidae by lacking the typical articular border on the lateral surface of the periotic and the anterior spine and the convex anterior border in the tympanic bulla. Furthermore, even though the squalodelphinids share a thick zygomatic process of the squamosal with MGPT-PU 13881/1-2, they show a dorsal margin of the zygomatic process of squamosal that is rounded in the lateral view, and the zygomatic process of the squamosal is partially superimposed on the postorbital process of the frontal. Finally, in squalodelphinids, teeth are conical and also occur on the proximal portion of the maxilla; despite the incompleteness of the maxilla in MGPT-PU 13881/1-2, careful examination of the fossil clearly indicates that the teeth were originally absent on the proximal portion of the maxilla.

Xenorophiidae differs from MGPT-PU 13881/1-2, with a more protruding and massive lateral tuberosity of the periotic and a tympanic bulla with protruding lobes separated by a broad median furrow; in addition, the ventral wall of the involucrum is characterized by a posterior protrusion. The skull of xenorophiids differs from MGPT-PU 13881/1-2, with

a falciform process of the squamosal that is much more prominent and pointed, with the zygomatic process not in contact with the postorbital process of the frontal. This feature is also shared by *Ankylorhiza tiedemani*.

Otekaieka differs from MGPT-PU 13881/1-2 by its comparatively longer anterior process of the periotic and smaller and thinner posterior process of the periotic, and a more symmetrical involucrem of the tympanic bulla; moreover, *Otekaieka* has a thin falciform process of the squamosal bone that forms a right angle, and a rounded skull with a comparatively narrower base of the rostrum. Finally, *Chilcacetus* differs from MGPT-PU 13881/1-2 by having a longer and thinner posterior process of the periotic; *Chilcacetus* possesses a zygomatic process of the squamosal bone that is more elongated anteriorly and moderately elevated towards the postorbital process of the frontal with which it is barely in contact. Moreover, the angle between the posterior process and the anterior process of the periotic of *Chilcacetus* is *c.* 120° rather than *c.* 90° as in MGPT-PU 13881/1-2. However, it is interesting to note that *Chilcacetus* shares the presence of a long and deep fovea epitubaria of the anterior process with MGPT-PU 13881/1-2; in the dorsomedial view, the anterior process of the periotic is slightly swollen transversely towards its base, with a more convex ventromedial margin than in most Eurhinodelphinidae, but with a lateral tuberosity similar in shape and direction; in addition, *Chilcacetus* further resembles MGPT-PU 13881/1-2 in sharing the presence of a falciform process of the squamosal with a massive zygomatic process.

5.2. Comparisons with Other Eurhinodelphinids

The presence of the fovea epitubaria in the anterior process of the periotic, the anterior process of the periotic bearing two articular facets for the tympanic bulla, the periotic with a round pars cochlearis with a smooth anterior surface, and comparable sizes of the pars cochlearis and the anterior process (1:1 ratio: [19,31,43,44]) clearly support the inclusion of MGPT-PU 13881/1-2 within the Eurhinodelphinidae. The neurocranium and proximal portion of the rostrum in the dorsal view of the majority of the eurhinodelphinid taxa described up to now are represented in Figure 16. As shown, the presence of a well-developed antorbital process of the frontal and a narrow and deep antorbital notch is shared by MGPT-PU 13881/1-2 and *Eurhinodelphis bossi*, *E. cocheteuxi*, *E. longirostris*, *Mycteriacetus*, *Ziphiodelphis abeli*, and *Z. sigmoideus*. The lack of the premaxillae from MGPT-PU 13881/1-2 prevents further comparisons with the rostrum. Additional observations can be performed in the periotic (Figure 17). The periotic of MGPT-PU 13881/1-2 resembles that of *Ziphiodelphis abeli* and *Xiphiacetus cristatus* with a triangular, robust, and inflated anterior process in dorsal view, and in the shape and size of the lateral tuberosity. The skull MGPT-PU 13881/1-2 resembles *Eurhinodelphis cochteauxi* and *Xiphiacetus cristatus* by having a reduced epitympanic hiatus and in the presence of an anterodorsal corner in the body of the periotic (in *Ziphiodelphis abeli*, the anterodorsal corner is not observed as this portion is flattened in dorsal view). Unfortunately, no periotic was described in the material of *Ziphiodelphis sigmoideus*, thereby excluding any possible comparative analysis concerning this anatomical district.

In the lateral view, the resemblance of the squamosal of MGPT-PU 13881/1-2 and that of *Ziphiodelphis sigmoideus* is observed. Detailed photographic plates showing the squamosal of *Ziphiodelphis sigmoideus* were published in ref. [9]. The anterodorsal portion of the zygomatic process of the squamosal in this species is characterized by an inflated and globular part that makes contact with the postorbital process of the frontal (see also Figure 18). The anteroventral portion is characterized by an articular facet squared in the lateral view, which serves the articulation with the jugal bone. Taken together, these two structures provide the anterior border of the zygomatic process of the squamosal of *Ziphiodelphis sigmoideus*, a squared anterior outline, and a robust appearance. The same outline is matched by the zygomatic process of the squamosal of MGPT-PU 13881/1-2.

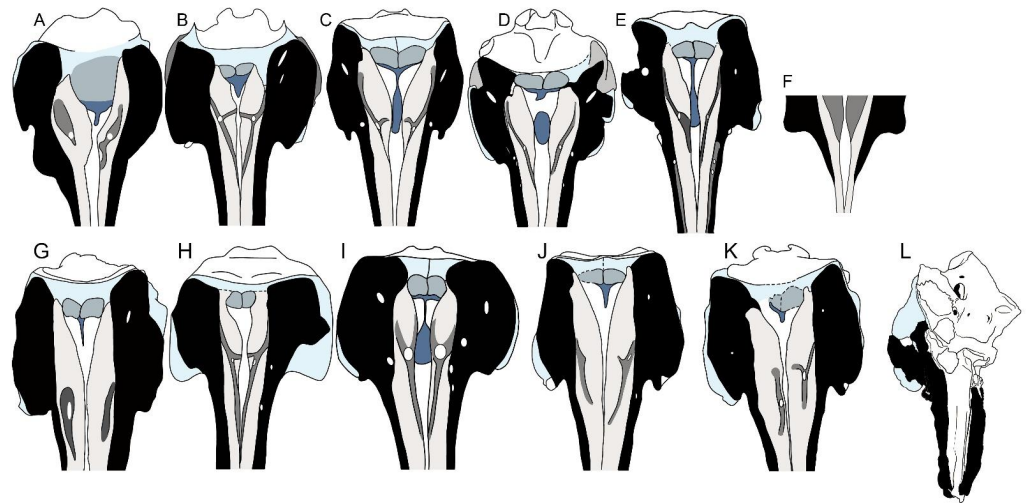


Figure 16. Schematic representation of posterior portions of eurhinodelphinid skulls in dorsal view. Not to scale. (A) *Iniopsis caucasica*. (B) *Eurhinodelphis bossi*. (C) *Eurhinodelphis cocheteuxi*. (D) *Eurhinodelphis longirostris*. (E) *Schizodelphis morckhoviensis*. (F) *Vanbreenia trigonia*. (G) *Mycteriacetus bellunensis*. (H) *Schizodelphis sulcatus*. (I) *Xiphiacetus cristatus*. (J) *Ziphiodelphis abeli*. (K) *Ziphiodelphis sigmoideus*. (L) MGPT-PU 13881/1, *Ziphiodelphis sigmoideus*.

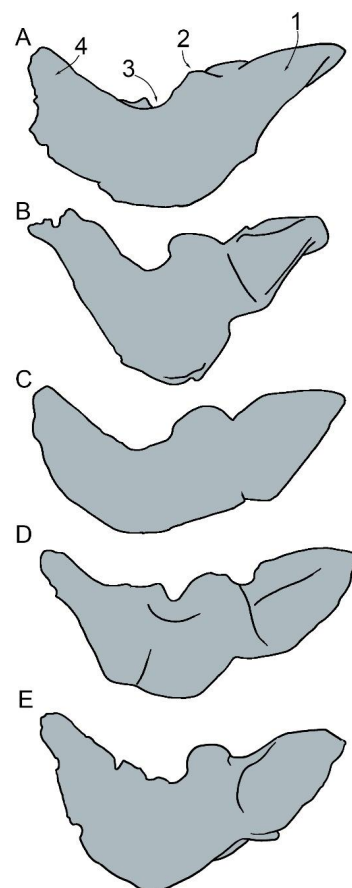


Figure 17. Morphology of eurhinodelphinid periotics in dorsal view showing selected characters used in phylogenetic analysis and comparisons. Caption: 1, size of anterior process; 2, size and shape of lateral tuberosity; 3, width of epitympanic hiatus; 4, size and shape of posterior process. Not to scale. (A) *Eurhinodelphis longirostris*. (B) *Eurhinodelphis cocheteuxi*. (C) *Ziphiodelphis abeli*. (D) *Xiphiacetus cristatus*. (E) *Ziphiodelphis sigmoideus* (MGPT-PU 13881/2).

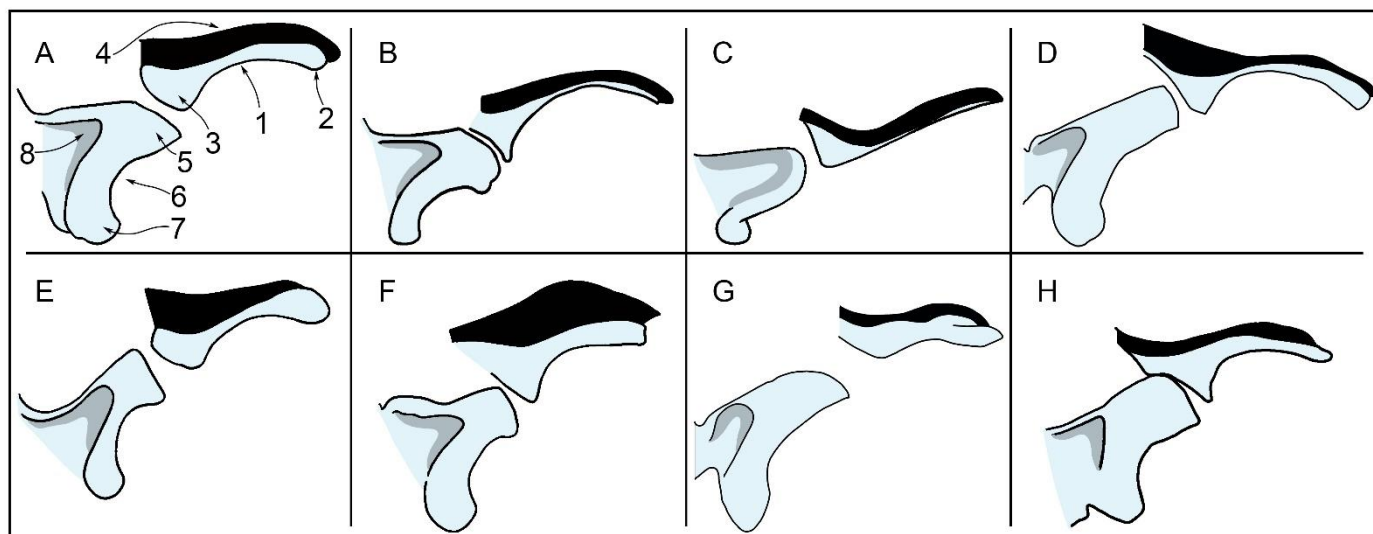


Figure 18. Comparative schemes showing the zygomatic process and the orbit in lateral views to illustrate some of the characters used in the phylogenetic analysis and comparisons sections. 1, thickness of orbital portion of the supraorbital process of the frontal; 2, size of antorbital process; 3, size of postorbital process; 4, relative thickness of maxilla covering of supraorbital process of frontal; 5, shape of anterior end of zygomatic process of frontal; 6, concavity and elongation of glenoid fossa of squamosal; 7, morphology of postglenoid process of squamosal; 8, depth of fossa for sternocephalic muscle. Not to scale. (A) *Eurhinodelphis cocheteuxi*. (B) *Eurhinodelphis longirostris*. (C) *Schizocetus sulcatus*. (D) *Mycteriacetus bellunensis*. (E) *Eurhinodelphis morckhoviensis*. (F) *Xiphiacetus cristatus*. (G) *Ziphiodelphis abeli*. (H) *Ziphiodelphis sigmoideus*.

All the other eurhinodelphinid species exhibit a more delicate anterior border of the zygomatic process of the squamosal. Additional differences with other eurhinodelphinid species were coded in the matrix used for phylogenetic analysis and will be discussed in the Phylogenetic analysis section based on a study of the distribution of the synapomorphies at the nodes.

In summary, the comparative analysis discussed herein supports the attribution of MGPT-PU 13881/1-2 to *Ziphiodelphis sigmoideus*. Consequently, MGPT-PU13881/1-2 provides detailed information on the anatomy of the periotic of this species that was previously unknown.

5.3. Neuroanatomical Comparisons

The endocast of MGPT-PU 13881/1-2 is compared herein with the natural endocasts of *Schizodelphis* [45], with a natural endocast of a Burdigalian odontocete published by [14] known with the catalogue number MGPT-PU 13873, and with a *Prosqualodon* endocast recently described [46]. Additional comparisons with other specimens are also provided.

In the ventral view, the general morphology of the endocast of MGPT-PU 13881/1-2 shows scarce development of the pons with respect to the *Schizodelphis* endocasts. In MGPT-PU 13881/1-2, the roots for the nerves entering the cranial hiatus (cranial nerves VII-XI) are transversely wider than in *Schizodelphis*, and the root of the trigeminal nerve shows a more conical appearance. Judging from the published illustrations [42], the foramen for the internal carotid artery is transversely closer in *Schizodelphis* and the hypophysis appears wider and more protruding. An additional difference is related to the bigger root of the trigeminal nerve in the natural endocasts of *Schizodelphis* and the trigeminal nerve that forms large, cylindrical structures running toward the anterior portion parallel to the longitudinal axis of the endocast. In both MGPT-PU 13881 and the natural endocasts of *Schizodelphis*, the optic chiasm has a comparable relative size. In the lateral view, the temporal lobe shows a similar morphology in both MGPT-PU 13881 and the natural endocasts of *Schizodelphis*,

with the trace of the sylvian fissure more developed in the former suggesting a higher degree of horizontal development of this structure with respect to the natural endocasts of *Schizodelphis*. Unfortunately, we have no information on the cerebellar morphology in MGPT-PU 13881.

With respect to MGPT-PU 13873, we observe a similar size and shape of the roots for the nerve entering the cranial hiatus and a smaller pons compared to the natural endocasts of *Schizodelphis*. The internal carotid arteries are well-spaced with respect to the transverse axis of the brain in both MGPT-PU 13873 and MGPT-PU 13881/1-2, but the root for the trigeminal nerve is more elongated anteroposteriorly and transversely narrow in the former. In this sense, MGPT-PU 13881/1 shows the smaller root for the trigeminal nerve among the endocasts examined herein for comparative purposes. The optic chiasm of MGPT-PU 13873 is comparatively smaller than that of MGPT-PU 13881/1-2, but the tract of the optic nerve (cranial nerve II) is comparatively wider in MGPT-PU 13873. In the lateral view, the temporal lobe of MGPT-PU 13873 shows an evident horizontally developed trace for the sylvian fissure with abundant vascularization. Such a development is less developed in MGPT-PU 13881/1-2. Moreover, the anteroventral corner of the temporal lobe is truncated in MGPT-PU 13873 and rounded in MGPT-PU 13881/1-2.

In a specimen referred to as aff. *Prosqualodon davidis*, the sylvian fissure is horizontally elongated and marks a well-developed dorsal border of the temporal lobe [46]. This characteristic is present in archaic odontocetes (e.g., eurhinodelphinids, xenorophiids such as *Albertocetus*, and *Prosqualodon*) but absent in extant species in which the sylvian fissure is limited to a dorsoventral sulcus that does not show any anteroposterior development [38]. Interestingly, in the specimen referred to as aff. *Prosqualodon davidis*, the anterior-most portion of the frontoparietal lobe is longer than the temporal lobe [46] showing a morphological pattern that is the opposite with respect to MGPT-PU 13873 and the balaenopterid *Marzanoptera tersillae* [47] from the Italian Pliocene. The endocast of aff. *Prosqualodon davidis* shows several peculiar characteristics such as a particularly elongated posterior portion of the frontoparietal lobe, a comparatively long and low temporal lobe, and an apparently reduced anteroposterior elongation of the cerebellum that suggests wide neural diversity among early odontocetes. Unfortunately, the ventral surface of that specimen was not described, and no further comparisons can be made.

Four views of the 3D rendering of the skull endocast of *Eurhinodelphis morrisi* were published without providing a formal description in a general study on modern visual techniques [48]. In this specimen, the sylvian fissure has clear horizontal development and is marked by a deep sulcus. The temporal lobe is apparently elongated but low showing a considerable difference with MGPT-PU 13881/1-2 and other odontocete species (see a comparative illustration in ref. [46]). In this context, the temporal lobe of MGPT-PU 13881/1-2 shows more advanced characters than that of *Eurhinodelphis morrisi*, and this is in agreement with the more basal position of the genus *Eurhinodelphis* hypothesized in previous phylogenetic studies [18,44] and in the present work.

The hypothalamus quotient of MGPT-PU 13881/1-2 is 0.122, a high value that falls within the range of some living mysticetes and matches that of *Schizodelphis sulcatus* and MGPT-PU 13873 ([14] and literature therein). Following the suggestion of Bisconti et al. (2021d,e) and Pilleri and Gühr (1970), a high value of the hypothalamus quotient suggests scarce development of the interpeduncular fossa and reduced internal mesencephalic flexure of the brain [14,47,49]. This suggests a less round morphology of the cerebral hemispheres for MGPT-PU 13881/1-2. In fact, the hypothalamus quotient calculated for MGPT-PU 13881/1-2 is the highest ever calculated for a crown cetacean species, suggesting that the brain of eurhinodelphinids retained this primitive character and supporting the view expressed in ref. [14] that a mesencephalic flexure evolved later in odontocete evolution.

6. Phylogenetic Analysis

The phylogenetic analysis resulted in the discovery of 11 equally parsimonious cladograms; after performing bootstrap and symmetric resampling supporting analyses, the

resulting 50% majority rule strict consensus tree is shown in Figure 19 against a temporal scale and with the indication of stratigraphic durations of the species. The tree length of the strict consensus tree is 110 steps, the CI is 0.445, the RI is 0.614, and the HI is 0.555. In the strict consensus tree, *Waipatia*, *Squalodon*, and *Eoplatanista* represent a sequence of non-eurhinodelphinid species positioned close to the root. The monophyly of *Squalodon* + the other ingroup taxa received bootstrap support and symmetric resampling values of 100. The monophyly of *Eoplatanista* + the other ingroup taxa received both a bootstrap support value and a symmetric resampling value of 73. Interposed between the monophyletic Eurhinodelphinidae and these taxa is a monophyletic group including *Iniopsis* and *Chilcacetus*.

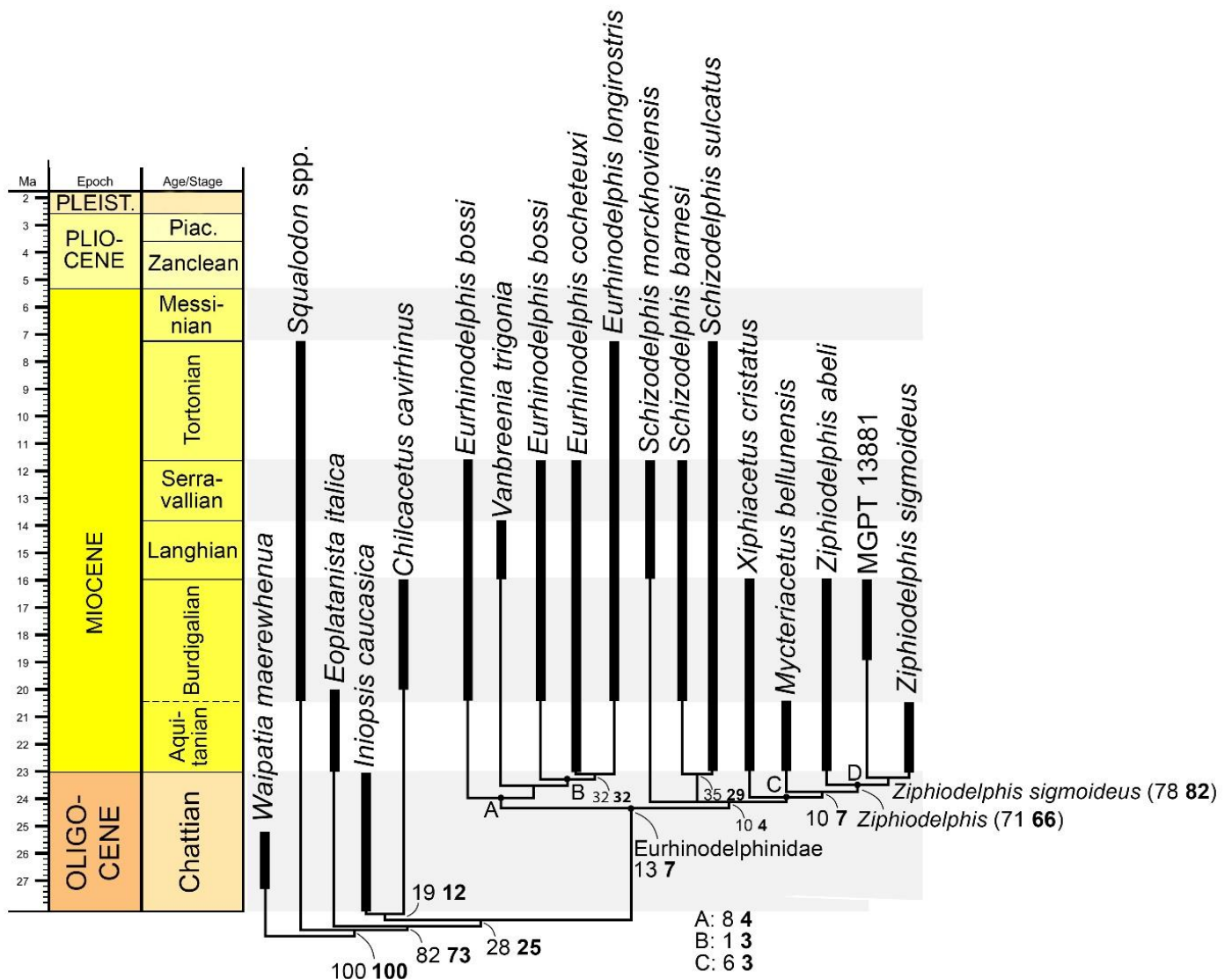


Figure 19. Phylogenetic relationships of Eurhinodelphinidae plotted against a temporal scale. Bold numbers represent bootstrap support values; regular numbers represent symmetric resampling supporting values.

In the strict consensus tree, the Eurhinodelphinidae is monophyletic but received too low bootstrap and symmetric resampling values so these values are not shown in Figure 19. Our results suggest that a monophyletic group including *Vanbreenia* + *Eurhinodelphis* (clade A in Figure 19) represents the basal-most eurhinodelphinid clade. *Eurhinodelphis* is monophyletic (clade B in Figure 19), and this confirms the results of early accounts on

this genus [18,19,44]. clade A is the sister group of a large clade including *Mycteriacetus*, *Xiphiacetus*, *Schizodelphis*, *Ziphiodelphis*, and MGPT-PU 13881/1-2 (clade C in Figure 19). The monophyly of *Ziphiodelphis* (clade D in Figure 19) received a bootstrap support value of 66 and a symmetric resampling value of 71. The monophyly of *Ziphiodelphis sigmoideus* + MGPT-PU 13881/1-2 received a bootstrap support value of 82 and a symmetric resampling value of 78, which is fully adequate to support the attribution of MGPT-PU 13881/1-2 to the species *Ziphiodelphis sigmoideus*.

In many cases, the bootstrap and symmetric resampling supporting values are lower than 50, suggesting scarce morphological support for a number of nodes. These include the monophyly of *Schizodelphis* and *Eurhinodelphis* and the monophyly of Eurhinodelphinidae itself. These low supporting values strongly suggest performing further and more detailed morphological samplings of these cetaceans in order to better solve the phylogenetic relationships of eurhinodelphinids. As shown in Supplementary Figure S3, the synapomorphies supporting each node are not numerous, and this depends on the generally low number of character states used for phylogenetic inference among Eurhinodelphinidae. In this paper, we added a number of morphological characters to the dataset [18], but further work is certainly necessary to better represent the morphological diversity of eurhinodelphinids in future phylogenetic datasets.

Apart from the problem of the low supporting values, we analyzed the frequency of occurrence of each clade in the strict consensus tree (Supplementary Figure S3 in Supplementary Material) and found that Eurhinodelphinidae is present in each of the 11 cladograms found by the implicit enumeration exact search (100% occurrence), and therefore also the two large clades found within Eurhinodelphinidae (*Vanbreenia* + *Eurhinodelphis* and the clade defined as *Schizodelphis* + clade C of Figure 19). Therefore, despite the low supporting value, it is still more parsimonious to maintain the monophyly of Eurhinodelphinidae valid than to consider Eurhinodelphinidae a paraphyletic entity. The sister group relationship between *Chilcacetus* + *Iniopsis* and Eurhinodelphinidae can be questioned as it occurred in only 45% of the cladograms found by the analysis of the present paper. This suggests that further work is necessary to better understand the phylogenetic position of these non-eurhinodelphinid taxa with respect to Eurhinodelphinidae.

Judging from our results, the origin of Eurhinodelphinidae should be placed in the earliest Aquitanian or the latest Chattian. The diversification into two clades (clades A and B in Figure 19) occurred very early in the history of this group, at the beginning of the Miocene. A subsequent diversification event occurred immediately later with the origin of the Mediterranean clade C. Apparently, the Eurhinodelphinidae underwent a sustained diversification at the latest Oligocene-earliest Miocene with no additional branches added to the group in the subsequent stages.

From a stratigraphic viewpoint, the agreement between the branching pattern of the cladogram and the stratigraphic age of the species as calculated by the SCI is $8/15 = 0.53$. This value suggests that only part of the stratigraphic intervals in which the taxa are recorded in the fossil record agrees with the branching order found in the cladogram of Figure 19. Likely, a better stratigraphic resolution for single species would help to increase the SCI value, but this would require a more refined analysis of the stratigraphic position of the species, which is beyond the scope of the present paper.

7. Paleobiogeographic Analysis

The reconstruction of ancestral geographic distributions at the nodes of the Eurhinodelphinidae family is shown in Figure 20. The ML algorithm implemented in Mesquite resulted in the discovery that the origin of Eurhinodelphinidae most likely occurred in the Northeast Atlantic with an ML probability value (hereinafter: MLPV) of 0.89. The Northeast Atlantic continued to represent the center of origin of several different clades including clade A (MLPV = 0.96), clade C (MLPV = 0.92), the genus *Eurhinodelphis* (MLPV = 0.97), and the clade including *Schizodelphis barnesi* + *S. sulcatus* (MLPV = 0.75). The origin of the genus *Ziphiodelphis* is less supported by fossil evidence, and we found only an MLPV

of 0.57, suggesting that this genus originated in the Northeast Atlantic and subsequently invaded the Mediterranean. Judging from our results, the presence of eurhinodelphinids in the Mediterranean, Northwest Atlantic, and Paratethys was the result of different dispersal events from a Northeast Atlantic center of origin.

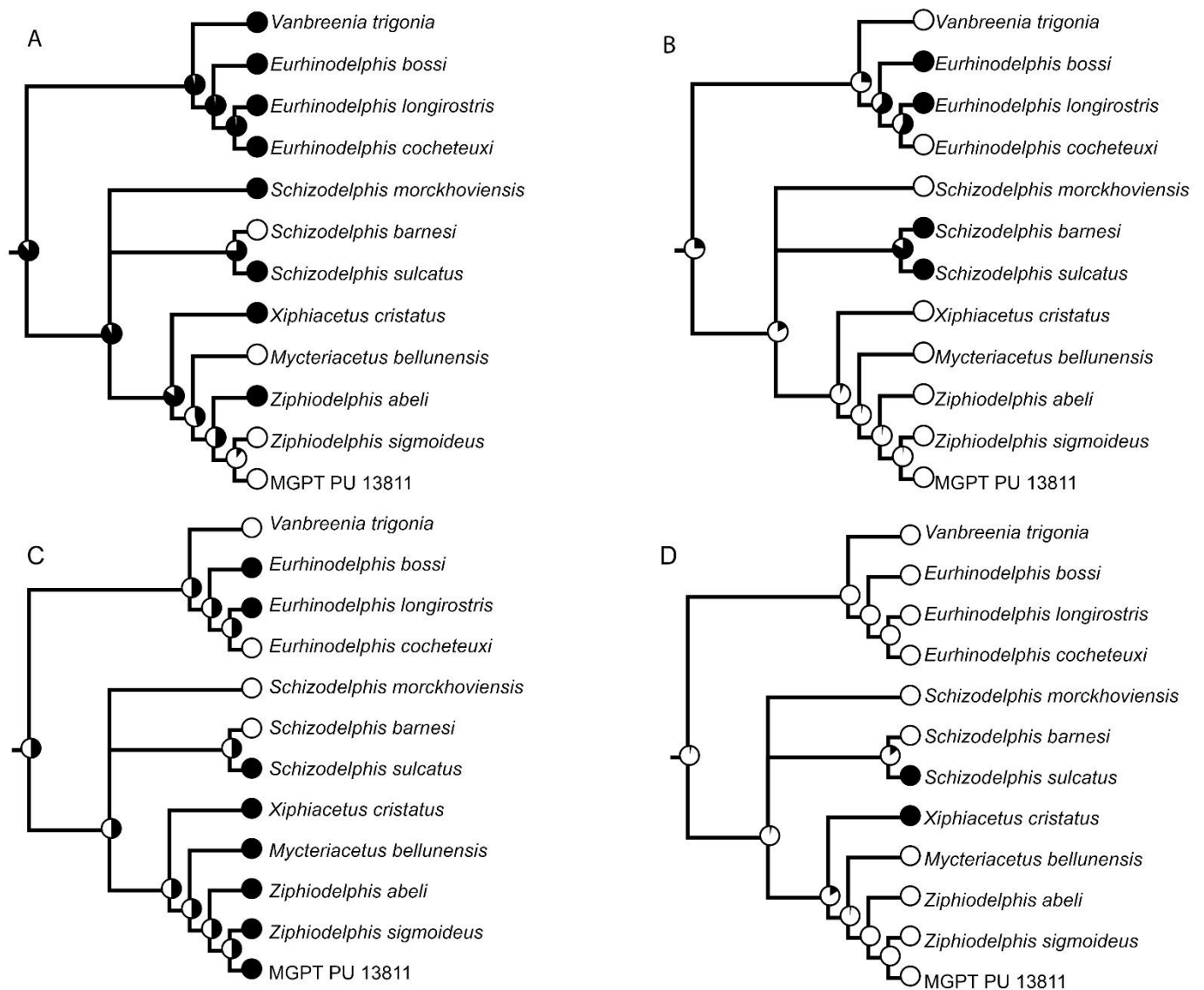


Figure 20. Paleobiogeographic relationships of Eurhinodelphinidae with reconstructions of ancestral geographic states at nodes. (A) Northeast Atlantic distributions. (B) Northeast Atlantic distributions. (C) Mediterranean distributions. (D) Paratethys distributions. Pie charts at internal nodes show ML probabilities of ancestral distributions.

8. Discussion

8.1. Morphology and Taxonomy of MGPT-PU 13881/1-2 and Revision of *Tursiops miocaenus*

The problems that emerged during the attempt to provide a detailed taxonomic assessment of MGPT-PU 13881/1-2 are the result of the incompleteness of the specimen. Most of the morphological characters useful for eurhinodelphinid taxonomy (i.e., the shape and relationships of the premaxilla with the frontal, supraoccipital, and nasal, morphology of the interorbital region of the frontal, teeth number, and distribution) are not preserved in the specimen, with negative implications for its identification. Diagnostic characteristics at the family level were identified in the ear bones, which therefore support the inclu-

sion of MGPT-PU 13881/1-2 within the family Eurhinodelphinidae. Then only a detailed comparison of the zygomatic process of the squamosal could resolve the taxonomic affinities of the specimen. This suggests that this skeletal structure may play a relevant but almost neglected role in the identification of clades within the Eurhinodelphinidae. We scored several new character states in the phylogenetic dataset we used to investigate the phylogenetic relationships of Eurhinodelphinidae, and the zygomatic process of the squamosal is represented in six of them. In particular, the shape of the anterior border of the zygomatic process of the squamosal was important as it may be slender or stocky, clavated, or truncated, and it may include an inflated anterodorsal portion and a squared anteroventral portion. These morphological details are thought to represent morphological diversity that was previously not discussed in detail.

Previous interpretations of the taxonomic affinity of MGPT-PU 13881/1-2 [1,6] were biased by the poor preservation state and incomplete preparation of the specimen.

As one of the specimens listed in [8] is *Tursiops miocaenus*, we attempted a revision of this taxon based on current evidence. Unfortunately, the species is based on six teeth that are now lost. The only evidence of this taxon is represented by a plate published by [8] that we reproduced in Figure 2. As shown, the teeth are morphologically simple; they show a pointed and conical apex and a uniformly curved proximal portion. There are no diagnostic characters observed in these teeth based on their illustrations made by [8]. For this reason, we are unable to provide a morphological diagnosis of *Tursiops miocaenus* and declare it a *nomen dubium*.

8.2. Phylogenetic and Paleobiogeographic Patterns in Eurhinodelphinidae

Our phylogenetic analysis expanded previous works on Eurhinodelphinidae by adding several taxa characteristics to the dataset. A previously published phylogenetic analysis [44] focused on the relationships of the Eurhinodelphinidae within the broader phylogeny of odontocetes. In that work [44], *Schizodelphis*, *Ziphiodelphis abeli*, and *Eurhinodelphis cocheteuxi* formed a sequence of sister taxa that were the sister group of Ziphiidae. *Waipatia* was considered their sister group. In a subsequent paper [50], it was suggested that the only eurhinodelphinid used in their analysis was the sister group of a large clade including Physeteroidea, Ziphiidae, and Delphinida, thereby supporting a more advanced position of Eurhinodelphinidae in the odontocete phylogeny. Subsequently, Lambert et al. (2019) included a unique eurhinodelphinid genus (i.e., *Xiphiacetus*) in a broad-scale, total evidence analysis of the odontocete families [51] with the result that it was the sister group of the platanistid *Zarhachis flagellator*, forming a clade that was the sister group of the whole Delphinida. Later, another work found that a monophyletic Eurhinodelphinidae clade was basal to a large Platanistoidea clade [52]. In summary, it is clear that the phylogenetic relationships of the Eurhinodelphinidae within the odontocete families are still not completely resolved. The large analysis published in ref. [51] was the only one that included more than one hundred operational taxonomic units and that produced well-supported results. Based on this assumption, a derived position for Eurhinodelphinidae should not be excluded. New and thorough analyses of the phylogenetic relationships of this group are crucial to assess its place within the evolutionary history of odontocetes.

As far as the intra-familial relationships of the eurhinodelphinid species are concerned, our results are largely consistent with those published in ref. [18] for a basal position of *Eurhinodelphis* in the phylogeny of the Eurhinodelphinidae. Moreover, we also support a close relationship between *Schizodelphis*, *Mycteriacetus*, *Xiphiacetus*, and *Ziphiodelphis*. Our results, however, show a more resolved branching order by identifying clades C (*Xiphiacetus* + *Mycteriacetus* + *Ziphiodelphis*) and D (*Ziphiodelphis abeli* and *Z. sigmoideus* including MGPT-PU 13881/1-2) and the clade including *Mycteriacetus* and *Ziphiodelphis*. We also found a close relationship between *Vanbreenia trigonia* and *Eurhinodelphis* confirming the eurhinodelphinid affinity of *Vanbreenia* that was previously suggested [53].

The phylogenetic results show a strong paleobiogeographic signal corresponding to different dispersal events in different basins primarily from the Northeast Atlantic.

This result is in agreement with a previously published preliminary paleobiogeographic analysis [44] in which it was found that the Northeast Atlantic (corresponding to the North Sea basin of his work) was the original geographic occurrence of a clade formed by the majority of the eurhinodelphinid genera (i.e., *Eurhinodelphis*, *Ziphiodelphis*, *Schizodelphis*, *Mycteriacetus*, and *Xiphiacetus*). Apparently, we do not find radiations after the invasion of a specific basin, rather, the occurrences of eurhinodelphinid species in different basins seem related to single dispersal events. Dispersal events occurred primarily during the transition from the latest Chattian to the earlier Aquitanian, suggesting a quick dispersal of the earliest eurhinodelphinid species with subsequent speciation events. A more detailed assessment of the stratigraphic ages of the known eurhinodelphinid species would certainly be useful for a better definition of the tempo of the dispersal events and evolutionary rates within this family.

8.3. Brain Evolution in Eurhinodelphinidae

The study of the morphological evolution of cetacean brains is still in its infancy despite a number of landmark works [54–56]. Apart from the work published by Pilleri and Gahr [45], only a few works have accounted for the morphology of natural and virtual endocasts of fossil cetaceans in recent years (e.g., [14,42,46,56]). A tentative synthesis of our knowledge of odontocete brain evolution was recently published [46] in which it is suggested that, during the evolution of toothed whales, a reduction of the extension of the sylvian fissure occurred at the transition of the Platanistidae + Ziphiidae + Delphinida clade that also includes the Eurhinodelphinidae. This reduction occurred in parallel to the increase in the depth of the interhemispherical fissure separating the cerebral hemispheres in more recent cetaceans including *Eurhinodelphis bossi*, a characteristic also observed in *Eurhinodelphis morrisi* based on the 3D rendering of the virtual endocast [48]. This characteristic is observed also in the natural endocast MGPT-PU 13873 [14].

While it is quite clear that the increase in the depth of the interhemispherical fissure occurred following the pattern published in ref. [46], the evolution of the shape of the sylvian fissure is not. Interestingly, the endocast MGPT-PU 13873 shows evidence of a posteriorly developed sylvian fissure and deep interhemispherical fissure, a pattern also observed in the extant genus *Platanista* [46]. This suggests that MGPT-PU 13873 could belong to a *Platanista*-like odontocete species, but this hypothesis is rejected by morphometric analyses [14]. In the end, the taxonomic affinities of MGPT-PU 13873 are still to be clarified, and new works on this endocast are necessary. It may be hypothesized that the similar morphologies observed in MGPT-PU 13873 and *Platanista* are dependent on convergent evolution due to the sharing of the same kind of fluvial habitat, but it is unclear how the depth of the interhemispherical fissure is related to these ecological characteristics.

The temporal lobe of MGPT-PU 13881/1-2 does not resemble that of squalodontid cetaceans [54] because it is much more rounded and inflated. It does not resemble that of *Albertocetus meffordorum* [57] since it is more developed, round, and inflated. It is reminiscent of that of *Schizodelphis* [45]. We hope that new works on the *Schizodelphis* endocasts will be carried out in the near future using modern visual and digital techniques in order to better represent the morphological characteristics of these important specimens and provide additional comparative information.

Very little is known of the evolution of the brain vasculature in cetaceans. Our interpretations of the morphology of the ventral surface of the virtual endocast of *Ziphiodelphis sigmoideus* MGPT-PU 13881/1 suggest that paired vertebral arteries are located in the posterior portion of the pons and that a basilar artery occupies the central portion of the pons along the sagittal axis of the brain. This suggests, in turn, that the basilar artery bifurcates at the anterior border of the pons giving rise to the posterior and anterior carotid arteries. This pattern resembles that observed in the narwhal, *Monodon monoceros* [58], which is compatible with the general pattern of ventral brain vasculature in vertebrates provided in [39] and the literature therein. A different pattern is observed in another cetacean species, i.e., the beluga, *Delphinapterus leucas*, in which the fusion of the vertebral arteries occurs

much more posteriorly, and the ventral surface of the pons is crossed by long and paired anterior and posterior carotid arteries [58]. None of these structures are visible in the virtual endocast of the bottlenose dolphin, *Tursiops truncatus* [40]. However, a long basilar artery running ventrally to the whole pons was documented in *Tursiops truncatus* [49], and this suggests that a posterior fusion of the vertebral arteries and a long basilar artery may be a primitive condition for odontocetes and, possibly, for Cetacea in general. The lack of data from archaeocetes and more basal odontocetes and mysticetes lowers the support for this inference, which has to be regarded with caution as it is largely speculative. From this discussion, it is evident that more work is necessary to better understand the evolution of brain vasculature in Cetacea.

9. Conclusions

The specimen MGPT-PU 13881/1-2 represents a partial skull of *Ziphiodelphis sigmoideus* to which the periotic MGPT-PU 13906 is also assigned. The taxonomic assessment was dependent on the occurrence of synapomorphic characteristics in the zygomatic process of the squamosal. In particular, both the holotype of *Ziphiodelphis sigmoideus* and MGPT-PU 13881/1-2 share a robust zygomatic process of the squamosal, which shows a truncated anterior end, a globular anterodorsal portion, and a squared anteroventral portion. These characteristics, together with additional ones, have been coded in a new phylogenetic analysis of the Eurhinodelphinidae that showed an early subdivision of this family into two different clades: One including *Vanbreenia* and *Eurhinodelphis* and the other including *Mycteriacetus*, *Xiphiacetus*, *Ziphiodelphis*, and *Schizocetus*. *Ziphiocetus* includes both *Z. abeli* and *Z. sigmoideus* (including MGPT-PU 13881/1-2). By adding MGPT-PU 13881/1-2 to *Ziphiodelphis sigmoideus*, for the first time, the previously unknown morphology of the periotic of this species has been described in detail.

Our results exclude that MGPT-PU 13881/1-2 and MGPT-PU 13906 belong to the genus *Tursiops* and allow us to consider the six teeth assigned by Portis [8] to this species that are currently lost as *nomen dubium*. We assign MGPT-PU 13881/3-4 to *Odontoceti incertae sedis* due to the lack of a clear association with the skull MGPT-PU 13881/1-2 and the lack of clear diagnostic characters at the family level.

Based on our phylogenetic results, most of the diversification of Eurhinodelphinidae occurred at the transition between the latest Oligocene and the earliest Miocene and derived from dispersal events from a Northeastern Atlantic center of origin. The invasion of the Northwest Atlantic, Mediterranean, and Paratethys by eurhinodelphinid species was thus the result of subsequent dispersal events from the Northeast Atlantic.

Virtual reconstruction of the skull endocast of MGPT-PU 13881/1-2 showed the sequence of roots for the cranial nerves and allowed for some comparative analyses. The ventral portion of the endocast of MGPT-PU 13881/1-2 differs from the corresponding part of *Schizodelphis* in a number of details; moreover, the temporal lobe of MGPT-PU 13881/1-2 differs from both *Schizodelphis* and *Eurhinodelphis morrisoni* (the only two eurhinodelphinid species for which images of skull endocasts are published) in terms of the degree of horizontal development of the Sylvian fissure and relative elongation. This work, therefore, illuminates a previously unknown neural diversity among Eurhinodelphinidae.

Supplementary Materials: The following supporting information can be downloaded at: <https://www.mdpi.com/article/10.3390/d15020227/s1>, Figure S1: The partial skull MGPT-PU 13881/1 before preparation. Figure S2: Position of the virtual endocast within the skull MGPT-PU 13881/1. Figure S3: Strict consensus tree found by the present analysis with indication of the synapomorphy distributions and the frequency of each clade in the 11 cladograms found by the implicit enumeration exact search; Table S1: Matrix used for phylogenetic analysis in Nexus format.

Author Contributions: In this work, V.T. and P.D. prepared the specimen; P.D. curated the specimen in the MPTA collection; R.D. provided the virtual endocast; V.T., R.D. and M.B. wrote the paper; V.T. measured the specimen; M.B. provided the illustrations and phylogenetic and paleobiogeographic analysis; R.D. provided Figure S2; V.T. and M.B. provided the comparative analysis; V.T., P.D., R.D.,

M.B., M.P. and G.C. contributed to the discussion; G.C. coordinated the group. All authors have read and agreed to the published version of the manuscript.

Funding: This research is supported by funds (ex-60%) from the Università degli Studi di Torino and by a contribution from MPTA.

Institutional Review Board Statement: Not applicable.

Informed Consent Statement: Not applicable.

Data Availability Statement: All data used in this research are published in the present paper, in the Supplementary Online Material associated with this paper that is published on the website of the journal, and in Morphosource (project: https://www.morphosource.org/concern/biological_specimens/000493295, accessed on 2 February 2023; 3D rendering of the skull: <http://n2t.net/ark:/87602/m4/493298>, accessed on 2 February 2023; 3D rendering of the virtual basicranium and endocast: <http://n2t.net/ark:/87602/m4/493301>, accessed on 2 February 2023).

Acknowledgments: The authors wish to thank Olivier Lambert very much for providing illustrations and bibliographic data for Eurhinodelphinidae and Toshiyuki Kimura for providing bibliographic information. This is publication number 367 of the Museo di Geologia e Paleontologia at the Università degli Studi di Torino. This work corresponds to part of the Master thesis of Vera Tosetto at the Università degli Studi di Torino. The authors want to express their warmest gratitude to the three anonymous referees that greatly improved the scientific content and the clarity of the manuscript and to the editorial office of *Diversity* for their constructive help.

Conflicts of Interest: The authors declare no conflict of interest.

Appendix A Dataset for Phylogenetic Analysis

Table A1. Description of character states used in the phylogenetic analysis.

N.	Character	State 0	State 1	State 2	State 3	Source
1	Mesorostral groove	Widely open at the level of the orbital notches	nearly closed			[19]
2	Concavity of the premaxillary sac fossa	Flat or weakly concave	Strongly concave			[19]
3	Transverse premaxillary crest	absent	present, giving the posterior extremity of the premaxilla a T-shape			[44]
4	Maxilla on the antorbital process in dorsal view	thin maxilla on the antorbital process	no maxilla	maxilla fully covers the antorbital process		[18]
5	Supraorbital crest (dorsal thickening of the maxilla above the orbit)	absent	Present			[18]
6	Roughly complete covering of the temporal fossa by the frontal-maxilla plate	no, squamosal widely visible in dorsal view	yes			[19]
7	Posterior margin of the maxilla goes beyond the anterior margin of the supraoccipital shield	no	Slightly beyond	Far beyond		[18] modified from [19]. Ordered character.
8	Vertical supraoccipital shield	no	yes			[30]
9	Height of occipital condyles	dorsal margin of condyles is lower than the basis of temporal fossa	dorsal margin of condyles is higher than the basis of temporal fossa	ventral margin of condyles is higher than the basis of temporal fossa		[18] modified from [19].

Table A1. Cont.

N.	Character	State 0	State 1	State 2	State 3	Source
10	Width of the vertex	ratio between minimum distance separating the maxillae across the vertex and postorbital width of the skull < 0.20	between 0.20 and 0.30	> 0.30		[19]
11	Proportions of the nasal	wider than long	as long as wide or longer than wide			[19]
12	Dorsal surface of the nasal	lower or at the same level than the frontal on the vertex	higher than the frontal without anterodorsal projection	projecting anterodorsally		[19]
13	Nuchal crest elevated and well defined	absent	present			[18]
14	Shape of the apex of postglenoid process of squamosal	progressively narrowing in a ventral direction	widening to form a rounded ventral tubercle			[44]
15	Height of the postglenoid process in lateral view	higher than the paroccipital process of the exoccipital	at the same height			[18]
16	Postglenoid process ventrally warped	no	yes			[18]
17	Height of the temporal fossa	ratio between height of the fossa and bizygomatic width > 0.30	c. 0.30			[19]
18	Contact between the lateral lamina of pterigoid and the falciform process of the squamosal	contact present	lamina laterally deflected and no contact			[18]
19	Fossa for the postorbital lobe of the pterygoid sinus on the orbit roof	no fossa reaching the orbit roof	small fossa laterally limited	longer fossa usually excavating at least half the width of the orbit roof		[19]
20	Pterygoid sinus excavating the falciform process	no	yes			[19]
21	Inner posterior prominence of the tympanic bulla	roughly as wide as the outer prominence in ventral view	distinctly narrower			[19]
22	Medial groove of the tympanic	rectilinear on the 2/3 of the bulla	exteriorly deflected	filled in	cross it anteroposteriorly	[18]
23	Tympanic bulla anteriorly pointed in ventral view, with a progressive narrowing	no, abrupt narrowing	yes			[19]
24	Anterior articular facet of the periotic	nearly flat or weakly excavated	wide and deep			[19]
25	Anterior angle of the periotic	Angle between pars cochlearis and anterior process > 70°	≤ 70°			[18]
26	Shape of the pars cochlearis of the periotic	trapezoidal to rectangular in ventral view	rounded especially anteromedially yes			[19]
27	Antorbital corners parallel or diverging from longitudinal axis of the skull in dorsal view	no	yes			This work
28	Antorbital notch size	wide	narrow			This work
29	Antorbital process length	short	protruding			This work
30	Distinctive convexity in posterior portion of premaxilla in dorsal view	absent	present			This work

Table A1. *Cont.*

N.	Character	State 0	State 1	State 2	State 3	Source
31	Comparative length of zygomatic process of squamosal	Longer than high	Shorter than high			This work
32	Shape of anterior border of zygomatic process of squamosal	clavated	trunkated			This work
33	Ventral projection of anterior border of zygomatic process of squamosal	no	Yes			This work
34	Length of orbit in comparison to length of glenoid fossa of squamosal	≤	>			This work
35	Large anterior process of periotic	yes	no			This work
36	Protrusion of lateral tuberosity of periotic	Scarce-to-absent	present			This work
37	Position of premaxillary foramen with respect to antorbital notch	More anterior	At least one foramen at level of antorbital notch	More posterior		This work
38	Anterodorsal portion of zygomatic process of squamosal transversely globular and inflated	no	yes			This work
39	Anteroventral portion of zygomatic process of squamosal flat and lower than anterodorsal portion	no	yes			This work

Table A2. Matrix used for phylogenetic and paleobiogeographic analyses. Note that the morphological dataset is included in characters 1–39. The last four characters (in light blue) represent occurrence data that were mapped onto the phylogenetic results and are not part of the morphological dataset. Therefore, the last four characters were not used for phylogenetic inference. The first five taxa of this matrix (*Waipatia maerewhenua*, *Squalodon* spp., *Eoplatanista italica*, *Chilcacetus cavirhinus*, and *Iniopsis caucasica*) are not included in Eurhinodelphinidae and were not coded for paleobiogeographic analysis.

Taxa	Character Numbers				
	1.	10.	20.	30.	40.
<i>Waipatia maerewhenua</i>	003100000	0100001000	0000000000	0000000000	---
<i>Squalodon</i> spp.	000000000	0000000000	0000010000	1010000000	---
<i>Eoplatanista italica</i>	000000211	2010111000	0021010???	0000?100??	---
<i>Chilcacetus cavirhinus</i>	120201100	1011???000	0001000011	1000110100	---
<i>Iniopsis caucasica</i>	00021111?	1??1??????	???????011	0?????????	---
<i>Schizodelphis barnesi</i>	010111111	2121100101	1101111???	???????????	0100
<i>Schizodelphis morckhoviensis</i>	010001211	2011110101	1111101100	0011110200	1000
<i>Ziphiodelphis abeli</i>	111001111	2021110111	1110101111	0000001200	1010
<i>Ziphiodelphis sigmoideus</i>	111001111	1021000111	1110??011	00100??211	0010
MGPT 13811	??00??1	??1??1??	?110101011	?010001?11	0010
<i>Xiphiacetus cristatus</i>	000011211	1101100112	1110111000	1111001200	1011
<i>Eurhinodelphis longirostris</i>	001201212	2000100110	0011100010	1111110200	1110
<i>Eurhinodelphis cocheteuxi</i>	001211212	2000100110	0011100011	1110111?00	1000
<i>Eurhinodelphis bossi</i>	001211212	2000100110	0011100001	00000??200	1110
<i>Mycteriacetus bellunensis</i>	110201211	21111001??	0110??0000	00100??100	0010
<i>Vanbreenia trigonia</i>	00?21????	???????????	?????????100	1??????2??	1000
<i>Schizodelphis sulcatus</i>	010101111	2111111101	1101111100	1100110100	1111

Table A3. Specimens coded for phylogenetic analysis and coding sources.

N.	Species	Specimens	Coding Sources
1	<i>Waipatia maerewhenua</i>	OU 22095	[18]
2	<i>Squalodon</i>	MHNL Dr15	[18]
3	<i>Eoplatanista italica</i>	MGPD 26409, MGPD 26408	[18]
4	<i>Chilcacetus cavirostris</i>	MNHN.F.PRU11	[59]
5	<i>Schizodelphis sulcatus</i>	MNHN RL 12, PGN 2	[18]
6	<i>Schizodelphis barnesi</i>	MNHN AMN 19	[18]
7	<i>Schizodelphis morckhoviensis</i>	IRSNB 3235-M.343	[18]
8	<i>Ziphiodelphis abeli</i>	MGPD 26390, MGPT 13881	This work
9	<i>Ziphiodelphis sigmoideus</i>	MGPD 26396	This work
10	<i>Xiphiacetus bossi</i>	USNM 8842	This work
11	<i>Xiphiacetus cristatus</i>	IRSNB 3234-M.361	[18]
12	<i>Eurhinodelphis longirostris</i>	MRHN 3249	This work
13	<i>Eurhinodelphis cocheteuxi</i>	IRSNB 3252-M.294	This work
14	<i>Mycteriacetus bellunensis</i>	MGPD 26404	[18]
15	<i>Iniopsis caucasica</i>	GM 116-121, 116-13-17	[60]
16	<i>Vanbreenia trigonia</i>	ZMA 17943	This work

References

- Bianucci, G. I cetacei fossili nei musei italiani. *Museol. Sci. Mem.* **2014**, *13*, 7–17.
- Damarco, P. I cetacei fossili del Museo Paleontologico Territoriale dell’Astigiano e del Monferrato in Asti. *Museol. Sci. Mem.* **2014**, *13*, 25–28.
- Bisconti, M.; Damarco, P.; Repetto, G.; Pavia, M.; Carnevale, G. Il Patrimonio Paleocetologico Piemontese: Storia E Prospettive. *Parva Nat.* **2021**, *15*, 15–58.
- Bianucci, G.; Landini, W. Change in diversity, ecological significance and biogeographical relationships of the Mediterranean Miocene toothed whale fauna. *Geobios Mém. Spéc.* **2002**, *24*, 19–28. [[CrossRef](#)]
- Mancin, N.; Pirini, C.; Bicchi, E.; Ferrero, E.; Valleri, G. Middle Eocene to Middle Miocene planktonic foraminiferal biostratigraphy for internal basins (Monferrato and northern Apennines, Italy). *Micropaleontology* **2003**, *49*, 341–358. [[CrossRef](#)]
- Pilleri, G.; Gahr, M.; Kraus, C. Odontoceti (Mammalia: Cetacea) from the lower Miocene of Rosignano, Piedmont, north Italy. *Investig. Cetacea* **1989**, *22*, 189–291.
- Parona, C.F. Nuovi fossili del Miocene di Rosignano Piemonte. *Atti R. Acc. Sci. Torino* **1916**, *51*, 963–968.
- Portis, A. Catalogo descrittivo dei Talassoterii rinvenuti nei terreni terziari del Piemonte e della Liguria. *Memorie Accad. Sci. Torino* **1885**, *37*, 247–365.
- Pilleri, G. The Miocene Cetacea of the Belluno sandstones (Eastern Southern Alps). *Mem. Sci. Geol.* **1985**, *36*, 1–87.
- Myrick, A.C. Variation, Taphonomy, and Adaptation of the Rhabdosteidae (=Eurhinodelphinidae) (Odontoceti, Mammalia) from the Calvert Formation of Maryland and Virginia. Ph.D. Thesis, (unpublished). University of California, Los Angeles, CA, USA, 1979.
- Fordyce, R.E. Rediscription of early Miocene dolphin *Phocaenopsis mantelli* Huxley, 1859 (Odontoceti, incertae sedis). *N. Z. J. Geol. Geophys.* **1981**, *24*, 563–568. [[CrossRef](#)]
- Muizon, C. Le polyphylétisme des Acrodelphidae, odontocètes longirostres du Miocène européen. *Bull. Mus. Natl. His. Nat.* **1988**, *4*, 31–88.
- Mead, J.G.; Fordyce, R.E. The therian skull: A lexicon with emphasis on the odontocetes. *Smiths. Contrib. Zool.* **2009**, *627*, 1–248. [[CrossRef](#)]
- Bisconti, M.; Damarco, P.; Tartarelli, G.; Pavia, M.; Carnevale, G. A natural endocast of an early Miocene odontocete and its implications in cetacean brain evolution. *J. Comp. Neurol.* **2021**, *529*, 1198–1227. [[CrossRef](#)] [[PubMed](#)]
- Evans, A.R.; Jones, D.; Boyer, A.G.; Brown, J.H.; Costa, D.P.; Morgan Ernest, S.K.; Fitzgerald, E.M.G.; Fortelius, M.; Gittleman, J.L.; Hamilton, M.J.; et al. The maximum rate of mammal evolution. *Proc. Natl. Acad. Sci. USA* **2012**, *109*, 4187–4190. [[CrossRef](#)] [[PubMed](#)]
- Silva, M.; Downing, J.A. The allometric scaling of density and body mass: A nonlinear relationship for terrestrial mammals. *Am. Nat.* **1995**, *145*, 704–727. [[CrossRef](#)]
- Fau, M.; Cornette, R.; Houssaye, A. Photogrammetry for 3D digitizing bones of mounted skeletons: Potential and limits. *CR Palevol.* **2016**, *15*, 968–977. [[CrossRef](#)]
- Benoit, J.; Adnet, S.; Welcomme, J.L.; Fabre, P.H. New skull of *Schizodelphis sulcatus* Gervais, 1861 (Mammalia, Odontoceti, Eurhinodelphinidae) from the Lower Miocene of Pignan (Hérault, France) and its implications for systematic of Eurhinodelphinidae. *Geobios* **2011**, *44*, 323–334. [[CrossRef](#)]
- Lambert, O. Review of the Miocene long-snouted dolphin *Priscodelphinus cristatus* du Bus, 1872 (Cetacea, Odontoceti) and phylogeny among eurhinodelphinids. *Bull. Inst. R. Sci. Nat. Belgique, Sci. Terre* **2005**, *75*, 211–235.

20. Goloboff, P.A.; Catalano, S.A. TNT version 1.5, including a full implementation of phylogenetic morphometrics. *Cladistics* **2016**, *32*, 231–238. [[CrossRef](#)]
21. Huelsenbeck, J.P. Comparing the stratigraphic record to estimates of phylogeny. *Paleobiology* **1994**, *20*, 470–483. [[CrossRef](#)]
22. Maddison, W.; Maddison, D. Mesquite: A Modular System for Evolutionary Analysis. 2019. Available online: <https://www.mesquiteproject.org/> (accessed on 8 December 2022).
23. Churchill, M.; Boessenecker, R.W.; Cementz, M.T. Colonization of the Southern Hemisphere by fur seals and sea lions (Carnivora: Otariidae) revealed by combined evidence phylogenetic and Bayesian biogeographical analysis. *Zool. J. Linn. Soc.* **2014**, *172*, 200–225. [[CrossRef](#)]
24. Bisconti, M.; Damarco, P.; Mao, S.; Pavia, M.; Carnevale, G. The earliest baleen whale from the Mediterranean: Large-scale implications of an early miocene thalassotherian mysticete from Piedmont, Italy. *Pap. Palaeontol.* **2021**, *7*, 1147–1166. [[CrossRef](#)]
25. Brisson, A.D. Regnum Animale in Classes IX Distributum, Sive Synopsis Methodica. In *Lugdum Batarorum, Apud.*; Theodorum Haak: Leiden, The Netherlands, 1762.
26. Uhen, M.D. New protocetid whales from Alabama and Mississippi, and a new cetacean clade, Pelagiceti. *J. Vert. Pal.* **2008**, *28*, 589–593. [[CrossRef](#)]
27. Fordyce, R.E.; De Muizon, C. Evolutionary history of cetaceans: A review. In *Secondary Adaptation of Tetrapods to Life in Water*; Mazin, J.-M., Buffrenil, D.V., Eds.; Verlag Pfeil: Munich, Germany, 2001; pp. 169–233.
28. Flower, W.H. Description of the skeleton of *Inia geoffrensis* and the skull of *Pontoporia blainvillei*, with remarks on the systematic position of these animals in the Order Cetacea. *Trans. Zool. Soc.* **1867**, *6*, 87–116. [[CrossRef](#)]
29. Abel, O. Les dauphins longirostres du Boldérien (Miocène supérieur) des environs d’Anvers. *Mém. Mus. R. Hist. Nat. Belgique* **1901**, *1*, 1–95.
30. Muizon, C. A new Ziphiidae (Cetacea) from the Early Miocene of Washington State (USA) and phylogenetic analysis of the major groups of odontocetes. *Bull. Mus. Natl. Hist. Nat.* **1990**, *12*, 279–326.
31. Lambert, O.; Wanzenböck, G.; Pfaff, C.; Louwye, S.; Kiriwet, J.; Marx, F.G. First eurhinodelphinid dolphin from the Paratethys reveals a new family of specialised echolocators. *Hist. Biol.* **2022**, 1–18. [[CrossRef](#)]
32. Dal Piaz, G. Sui vertebrati delle arenarie mioceniche di Belluno. *Atti Della Accad. Sci. Veneto-Trentino-Istriana* **1908**, *5*, 106–120.
33. Coletti, G.; Basso, D.; Frixia, A.; Corselli, C. Transported rhodoliths witness the lost carbonate factory: A case history from the Miocene Pietra da Cantoni limestone (NW Italy). *Riv. Ital. Paleontol. Stratigr.* **2015**, *121*, 345–368. [[CrossRef](#)]
34. Dela Pierre, F.; Piana, F.; Fioraso, G.; Boano, P.; Bicchi, E.; Forno, M.G.; Violanti, D.; Clari, P.; Polino, R. *Note Illustrative Della Carta Geologica D’Italia Alla Scala 1:50.000. Foglio 157 Trino*; APAT, Dipartimento Difesa del Suolo: Roma, Italy, 2003; p. 147.
35. Festa, A.; Dela Pierre, F.; Piana, F.; Fioraso, G.; Lucchesi, S.; Boano, P.; Forno, M.G.; Bicchi, E.; Violanti, D.; Trenkwalder, S.; et al. *Note Illustrative Della Carta Geologica D’Italia Alla Scala 1: 50.000 Foglio 156 Torino Est*; ISPRA, Dipartimento Difesa del Suolo: Roma, Italy, 2009; p. 143.
36. D’Atri, A.R.; Dela Pierre, F.; Festa, A.; Gelati, R.; Gnaccolini, M.; Piana, F.; Clari, P.; Polino, R. Tettonica e sedimentazione nel retroforeland alpino. In Proceedings of the 81° Riunione Estiva Della Società Geologica Italiana, Torino, Italy, 10–12 September 2002; pp. 83–86.
37. Ketten, D.R. The cetacean ear: Form, frequency, and evolution. In *Marine Mammal Sensory Systems*; Thomas, J., Kastelein, R., Supin, A., Eds.; Springer: New York, NY, USA, 1992; pp. 53–75. ISBN 978-1-4615-3406-8.
38. Cozzi, B.; Huggenberger, S.; Oelschläger, H. *Anatomy of Dolphins. Insights into Body Structure and Function*; Academic Press: London, UK, 2017; ISBN 9780124076556.
39. Rahmat, S.; Gillan, E. Comparative anatomy of the carotid-basilar arterial trunk and hindbrain penetrating arteries in vertebrates. *Open Anat. J.* **2014**, *6*, 1–26. [[CrossRef](#)]
40. Colbert, M.W.; Racicot, R.; Rowe, T. Anatomy of the cranial endocast of the bottlenose dolphin, *Tursiops truncatus*, based on HRXCT. *J. Mam. Evol.* **2005**, *12*, 195–207. [[CrossRef](#)]
41. Burrows, A.M.; Smith, T.D. Forms and patterns of the external aspect of the brain and the superficial dural venous sinuses of the river dolphins (Cetacea: Odontoceti) from endocasts and their bearing on phylogenetic reconstruction. *Ann. Carnegie Mus.* **2005**, *74*, 201–215. [[CrossRef](#)]
42. Racicot, R.A.; Rowe, T. Endocranial anatomy of a new fossil porpoise (Odontoceti, Phocoenidae) from the Pliocene San Diego Formation of California. *J. Ver. Pal.* **2014**, *88*, 652–663. [[CrossRef](#)] [[PubMed](#)]
43. Lambert, O. Systematic revision of the Miocene long-snouted dolphin *Eurhinodelphis longirostris* du Bus, 1872 (Cetacea, Odontoceti, Eurhinodelphinidae). *Bull. Inst. R. Sci. Nat. Belgique Sci. Terre* **2004**, *74*, 147–174.
44. Lambert, O. Phylogenetic affinities of the long-snouted dolphin *Eurhinodelphis* (Cetacea, Odontoceti) from the Miocene of Antwerp. *Palaeontology* **2005**, *48*, 653–679. [[CrossRef](#)]
45. Pilleri, G.; Gühr, M. The brain and cephalization of *Schizodelphis sulcatus* Gervais, 1861. *Inv. Cetacea* **1982**, *13*, 13–26.
46. Tanaka, Y.; Ortega, M.; Fordyce, R.E. A new early Miocene archaic dolphin (Odontoceti, Cetacea) from New Zealand, and brain evolution of the Odontoceti. *N. Z. J. Geol. Geophys.* **2022**, 1–15. [[CrossRef](#)]
47. Bisconti, M.; Daniello, R.; Damarco, P.; Tartarelli, G.; Pavia, M.; Carnevale, G. High encephalization in a fossil orqual illuminates baleen whale brain evolution. *Br. Behav. Evol.* **2021**, *96*, 78–90. [[CrossRef](#)]
48. Marino, L.; Uhen, M.D.; Pyenson, N.D.; Frohlich, B. Reconstructing cetacean brain evolution using computed tomography. *Anat. Rec. B* **2003**, *272B*, 107–117. [[CrossRef](#)]

49. Pilleri, G.; Gahr, M. The central nervous system of mysticete and odontocete whales. *Inv. Cetacea* **1970**, *3*, 89–128.
50. Lambert, O.; Bianucci, G.; Urbina, M. A new inioid (Cetacea, Odontoceti, Delphinida) from the Miocene of Peru and the origin of modern dolphin and porpoise families. *Zool. J. Linn. Soc.* **2017**, *179*, 919–946. [[CrossRef](#)]
51. Lambert, O.; Godfrey, S.J.; Fitzgerald, E.M.G. *Yaquinacetus meadi*, a new latest Oligocene-early Miocene dolphin (Cetacea, Odontoceti, Squaloziphiidae, fam. nov.) from the Nye mudstone (Oregon, USA). *J. Vert. Pal.* **2019**, *38*, e1559174. [[CrossRef](#)]
52. Bianucci, G.; Muizon, C.d.; Urbina, M.; Lambert, O. Extensive Diversity and Disparity of the Early Miocene Platanistoids (Cetacea, Odontoceti) in the Southeastern Pacific (Chilcatay Formation, Peru). *Life* **2020**, *10*, 27. [[CrossRef](#)]
53. Bianucci, G.; Landini, W. A new short-rostrum odontocete (Mammalia:Cetacea) from the middle Miocene of the eastern Netherlands. *Beaufortia* **2002**, *52*, 187–196.
54. Breathnach, A.S. Observations on endocranial casts of recent and fossil cetaceans. *J. Anat.* **1955**, *89*, 532–546.
55. Dart, R.A. The brain of the Zeuglodontidae (Cetacea). *Proc. Zool. Soc.* **1923**, *1923*, 615–654. [[CrossRef](#)]
56. Elliott Smith, G. The brain of the Archaeoceti. *Proc. Roy. Soc.* **1902**, *71*, 322–331.
57. Boessenecker, R.W.; Ahmed, E.; Geisler, J.H. New records of the dolphin *Albertocetus meffordorum* (Odontoceti: Xenorophidae) from the lower Oligocene of South Carolina: Encephalization, sensory anatomy, postcranial morphology, and ontogeny of early odontocetes. *PLoS ONE* **2017**, *12*, e0186476. [[CrossRef](#)]
58. Vogl, A.V.; Fisher, H.D. Arterial circulation of the spinal cord and brain in the Monodontidae (Order Cetacea). *J. Morphol.* **1981**, *170*, 171–180. [[CrossRef](#)]
59. Lambert, O.; Muizon, C.; Bianucci, G. A new archaic homodont toothed cetacean (Mammalia, Cetacea, Odontoceti) from the early Miocene of Peru. *Geodiversitas* **2015**, *37*, 79–108. [[CrossRef](#)]
60. Mchedlidze, G.A. General Features of the Paleobiological Evolution of Cetacea. Amerind Publishing, Co.: New Dehli, India, 1984.

Disclaimer/Publisher’s Note: The statements, opinions and data contained in all publications are solely those of the individual author(s) and contributor(s) and not of MDPI and/or the editor(s). MDPI and/or the editor(s) disclaim responsibility for any injury to people or property resulting from any ideas, methods, instructions or products referred to in the content.